ELECTROPLATING RF MEMS RESONATORS AND OPTICAL CHARACTERIZATION

by

Mohammad Hossein Mazaheri Kouhani

B.S., Electrical Engineering- Electronics,

University of Tehran , 2012

Submitted to the Institute for Graduate Studies in
Science and Engineering in partial fulfillment of
the requirements for the degree of
Master of Science

Graduate Program in Electrical and Electronics Engineering

Boğaziçi University

2014

ACKNOWLEDGEMENTS

First of all, I would like to thank my thesis supervisor Prof. Arda Deniz Yalçınkaya for involving me in this exciting project. His guidance, trust, and kindness throughout this study enabled me to develop my professional skills and define my research perspectives for future.

Secondly, I am grateful to Prof. Hamdi Torun for being very professional, kind, and helpful throughout my research. I would also like to thank Prof. Onur Ferhanoğlu for joining my thesis committee.

I express my warm thanks to Mr. Mustafa Kemal Ruhi and Mehmet Yumak for their great support during the fabrication process and Mr. Uraz Cakaci, Berk Camli, and Emre Kusakci for their helpful contribution in my entire work.

I want to show my appreciation to my parents, Dr. Hassan Mazaheri Kouhani and Simin Jemssi, and my dear sisters whom their sincere love has always kept me harmonious throughout the entire of my life.

I owe many special thanks to my dear partner, Duygu Bekli, that her affection, guidance, and encouragement has boosted my life and career.

In addition, I would like to thank The Scientific and Technological Research Council of Turkey (TÜBİTAK) for providing scholarship throughout my study. This project is supported by TÜBİTAK, grant EEEAG 111E197.

Finally, I use this opportunity to express my gratitude to everyone who supported me throughout the course of this Master thesis. I am thankful for their guidance, invaluably constructive criticism and friendly advice during the project work.

ABSTRACT

ELECTROPLATING RF MEMS RESONATORS AND OPTICAL CHARACTERIZATION

Magnetic resonance imaging (MRI) is an advantageous imaging platform for endovascular interventions due to its higher safety and performance comparing with other imaging techniques. Localization of the catheter under MRI requires the employment of external devices. Among the various solutions in literature, electromagnetic tracking systems (EMTS) are advantageous due to their ease of use, safety, small size, and relatively high accuracy. They typically utilize conductive wiring for the transmission of electrical signal. However, under MRI radio frequency (RF) magnetic fields induce heat in conductive materials. This thesis presents fabrication, and characterization of RF MEMS-based electromagnetic resonators designed to be integrated with a MRI-compatible catheter tracking system. The tracking system is designed to communicate with fiber optic cables eliminating the use of conductive materials. MEMS resonators act as transducer to convert the electrical signal to displacement using the mechanical force induced by Lorentz force. The devices are designed such that the vibration can be detected either via laser Doppler vibrometry (LDV) and/or via diffraction grating interferometry (DGI). The resonance frequencies of a family of devices are investigated by finite element method (FEM) simulation. The range of frequency for the MEMS sensor array is from 145 kHz to 1.48 MHz. Devices are fabricated using electroplating nickel onto a seed layer of copper on a silicon substrate and characterized by LDV. The characterization setup provides a magnetic field of 0.62 Tesla which is generated by two parallel cubic permanent magnets. The characterization results show that the MEMS resonators are able to resonate by having a 10 dB of signal-to-noise ratio (SNR) at the electrical current of 25 μA (RMS). Experimental results prove that the devices are ready to function in the real-world application.

ÖZET

RF MEMS ÇINLAYICILARIN ELECTROKAPLAMASI VE OPTİK BELİRLEMESİ

Manyetik rezonans görüntüleme (MRG), diğer görüntüleme tekniklerine kıyasla sahip olduğu yüksek başarım ve güvenlik sebebiyle üstünlüklü bir görüntüleme platformudur. MRG'de kateter yerinin belirlenmesi harici cihazların kullanılmasını gerektirir. Literatürdeki çeşitli çözümler arasında yer alan elektromanyetik takip sistemleri (EMTS) kolay kullanım, güvenlik, küçük boyut ve görece yüksek kesinlikleri ile üstünlüklüdür. Bunlar genellikle elektriksel işaretlerin iletimi için iletken kablolara sahiptirler. Öte yandan, MRG radyo frekans (RF) manyetik alanları iletken kablolarda ısınmaya sebep olmaktadır. Bu tez, bir MRG uyumlu kateter takip sistemine tümleştirilmek üzere tasarlanmış RF MEMS tabanlı elektromanyetik çınlayıcıların üretim ve ölçümünü sunmaktadır. Takip sistemi, iletken malzemelerin kullanımını ortadan kaldıran fiber optik kablolar ile iletişim kurmak üzere tasarlanmıştır. MEMS çınlayıcılar, Lorentz kuvveti olarak ortaya çıkan mekanik etkiyi kullanarak elektriksel işareti yer değiştirmeye çeviren bir dönüştürücü işlevi görür. Yapılar, titreşimleri lazer Doppler titreşimölçümü (LDT) ve/ya kırınım ızgarası girişimölçümü (KIG) sayesinde algılanabilecek şekilde tasarlanmıştır. Bir yapı ailesinin çınlama frekansları sonlu eleman analizi (SEA) benzetimleri ile incelenmiştir. MEMS algılayıcı dizisi için frekans aralığı 145 kHz ile 1.48 MHz arasındadır. Yapılar silikon bir alttaş üzerinde, çekirdek bir bakır katmanın nikel ile galvanize kaplanması ile üretilmiş ve LDT ile belirlenmiştir. Belirleme düzeneği, kübik iki koşut sabit mıknatıs tarafından üretilen 0.62 Tesla kadar bir manyetik alan sağlar. Belirleme sonuçları MEMS çınlayıcıların 25 μA rms değerinde bir elektrik akımda 10 dB'lik bir işaret-gürültü oranı ile çınlayabildiğini göstermiştir. Deney sonuçları, yapıların gerçek dünya uygulamalarında işlev gösterebileceğini göstermektedir.

TABLE OF CONTENTS

LIST OF FIGURES

LIST OF TABLES

LIST OF SYMBOLS

a	Diffraction grating width
B_0	DC magnetic field
b	Gap width between the diffraction gratings
B_{Grad}	Gradient magnetic field
E	Young's modulus
F_0	Supporting force
f_{FID}	The frequency of FID signals
f_{Larmor}	Larmor frequency
F_L	Lorentz force
f	Resonant frequency
fw	Width of the flexure
g	Gravitational acceleration
i	Electrical current
I_{YY}	Second moment of inertia with respect to the y-axis
K_s	Spring constant due to out-of-plane force
l_r	Total length of resonator
lf	Length of the flexure
lm	Length of the mirror
m_0	Restrictive moment
M_{eff}	Effective weight
M_f	Mass of the resonator flexure
M_m	Mass of the resonator mirror
M_t	Total mass
M_{XY}	Net magnetization in transverse direction
M_Z	Net magnetization in longitudinal
mw	Width of the mirror
p	the length of beam's flexure
q	the width of beam's flexure

t	thickness of the MEMS resonator structural layer
w	Displacement function in the out-of-plane direction

LIST OF ACRONYMS/ABBREVIATIONS

2D	Two dimensional
3D	Three dimensional
AC	Alternating current
CCD	Charge-coupled-device
CMOS	Complementary Metal Oxide Semiconductor
CT	Computerized tomography
CTE	Coefficient of thermal expansion
DC	Direct current
DGI	Diffraction grating interferometry
EPI	Electronic portal images
EMTS	Electromagnetic tracking systems
FEM	Finite element method
FID	Free induction decay
FOV	Field of view
H	Hydrogen
IC	Integrated circuits
IR	Infrared
LDV	Laser Doppler vibrometry
LED	Light emitting diode
MEMS	Microelectromechanical systems
MR	Magnetic resonance
MRI	Magnetic resonance imaging
NIR	Near infrared
NM	Nuclear magnetic
OTS	Optical tracking system
PET	Positron emission tomography
PCB	Printed circuit board
PR	Photo resist

RF	Radio frequency
RMS	Root mean square
SNR	Signal-to-noise ratio
UTS	Ultrasonic tracking systems
UV	Ultra violet
VTS	Videometric tracking systems
XF	X-Ray Fluoroscopy

1. INTRODUCTION

Among the major types of medical operation, minimally invasive diagnosis and treatment techniques are very advantageous, comparing with their invasice alternatives involving cutting the tissues in order to reach the internal organs. Among the major minimally invasive medical techniques, catheter based endovascular applications are of great importance and they are becoming more common with the advancement of new developments [14]. Catheters are biocompatible devices, which can be inserted into the body via certain ducts and/or blood vessels to perform various medical operations and provide surgical navigation. An essential component of endovascular interventional operations is localization of the catheter meaning that the location of the catheter inside the body should be tracked with a very high accuracy.

The major image-guided interventional tracking systems fall into four groups- optical tracking systems (OTS), image-based computational trackers, ultrasonic tracking systems (UTS), and electromagnetic tracking systems (EMTS).

1.1. Optical tracking systems

An OTS usually integrates one or many of charge-coupled-devices (CCD), infrared (IR) devices and/or light-emitting diodes (LED) with image-guiding systems. OTS usually have applications in orthopedics due to its high accuracy and reliability but they mainly suffer from deficiencies for the line-of-sight and large size compared with EMTS [2].

The broad use of OTS in industry has introduced many manufacturers and system variants with wide-ranging specifications. Clinical systems are a niche sector and the technology used for their operation has not changed significantly in recent years [12]. Optical tracking systems can be characterized into two main categories- videometric tracking systems (VTS) and IR-based tracking systems.

1.1.1. Videometric tracking systems

These systems identify markers on a series of video image sequences, usually taken using calibrated video cameras. The well-known marker patterns on crash-test dummies as well as the videometric solutions implemented in the VISLAN system (an integrated neurosurgical planning and guidance system [15]) and the freely available AR Toolkit [16] fall into this category. Figure 1.1 shows specific implementation of a video-based tracker using Claron MicronTracker. The C-arm is a prototype developed for high-quality intraoperative cone-beam CT. The mount places the tracker at 60 cm from isocenter and incorporates a Pb glass window to shield the tracker from radiation damage. The reference marker comprised six faces visible from 360 degrees to define a reference coordinate system enabling tracking across a full C-arm rotation. The localization of markers along with the registration of tracking devices enable a virtual fluoroscopy.

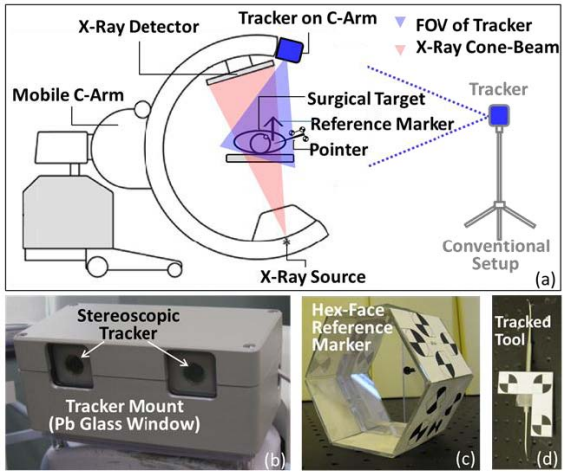

Figure 1.1. (a) Schematic of the Tracker-on-C and conventional tracker configurations. (b) Video-based tracker within the C-arm mount. (c) Hex-face reference marker allowing tracker registration within a dynamic reference frame. (d) An example tracked tool (surgical pointer) [1].

1.1.2. IR-based tracking systems

An optical band-pass filter can eliminate the undesired wavelengths and enable the detection of optical markers. The IR-based trackers fall into two main categories in terms of power consumption- active and passive.

Active IR-based catheters are formed of a number of LEDs operating in IR range which are used as markers. The markers are detected by the utilization of linear CCD units (see Figure 1.2). Since the LEDs need to be powered, traditionally, these systems are wired [2].

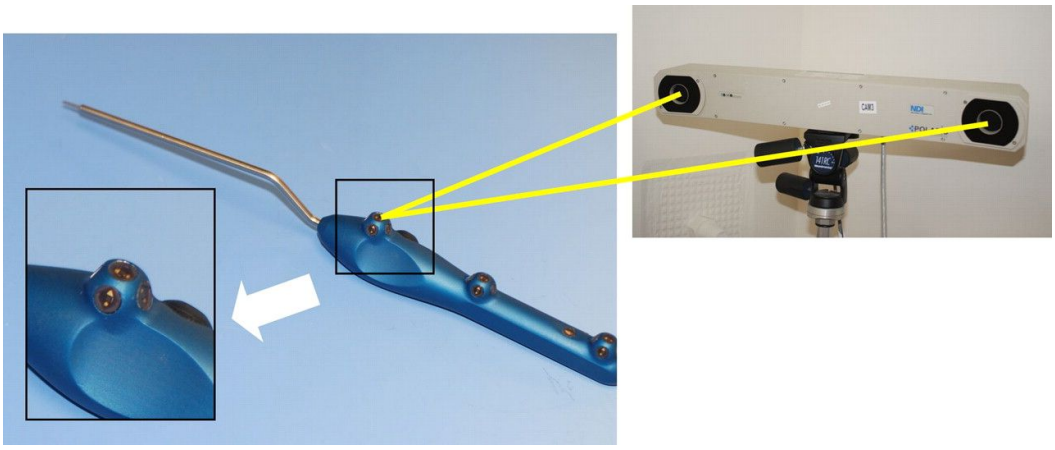

Figure 1.2. Active infrared tracker. Both lenses of the camera (Polaris; Northern Digital) must view at least three infrared light-emitting diodes on the probe handle (area shown within black box) to determine the location of the probe tip. This probe contains clusters of infrared light-emitting diodes to improve visibility [2].

Passive IR-based trackers work in the NIR range. In contrast to active IR-based trackers, retroreflective spheres [17] are illuminated by the camera in the near-IR spectrum. These systems are often equipped with 2D CCD cameras. A major advantage of passive systems is that no wires are needed between the tracking system and the detected probes [12]. Figure 1.3 shows an acquisition system based on NIR passive tracking.

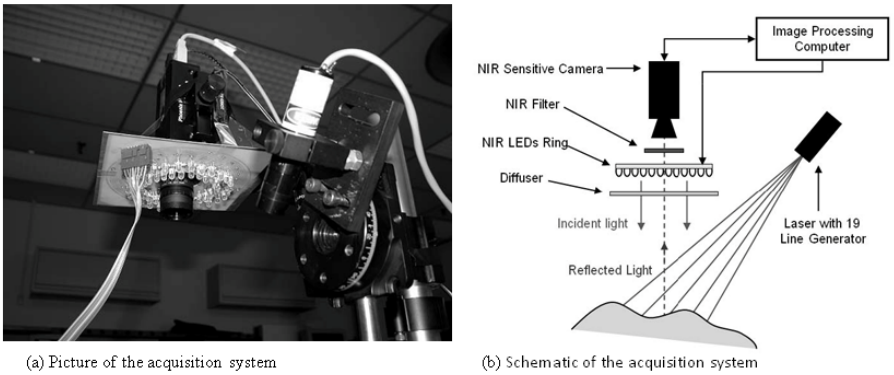

Figure 1.3. Picture and schematic of the acquisition system including a NIR sensitive camera, a NIR interferometric filter, a NIR multi-wavelength ring of LEDs and a NIR line-generating laser module [3].

1.2. Image-based computational techniques

Image-based computational techniques are type of passive tracking systems that employ two dimensional (2D) and three dimensional (3D) registration techniques typically under X- ray Fluoroscopy (XF) [18–21]. Figure 1.4 shows the experimental result of a tracking algorithm based on variational calculus. The differential euations deform a spline, subject to intrinsic and exrinsic forces, so that it matches the image data, remains smooth an a priori length [4].

Tumor motion detection by identifying the marker motion in electronic portal images (EPI) acquired during radiation therapy is another implementation of image-based tracking systems. In this type of techniques, the treatment beam is used as an imaging modality where the resulting absorption images resemble conventional x-ray imaging. One drawback of this technique is the poor image contrast provided by the high-energy photons emitted by the accelerator. Nevertheless, external or internal markers are easily detected in those perspective images. The markers are typically

radiopaque gold markers implanted to monitor prostate interfraction motion during radiation therapy [22–28]. Another similar technique is the tracking of guidewires or similar structures in XF images during radiological interventions [29, 30]. The localization of bronchoscopes from a comparison of virtual endoscopy images [31] and angiography images [32] are two other image-based computaional techniques.

As the registration techniques become faster with higher performance rendering techniques and computing capabilities using light fields [33–35], improved image-based tracking may soon become the technology of choice for a variety of applications in interventional image-guided procedures.

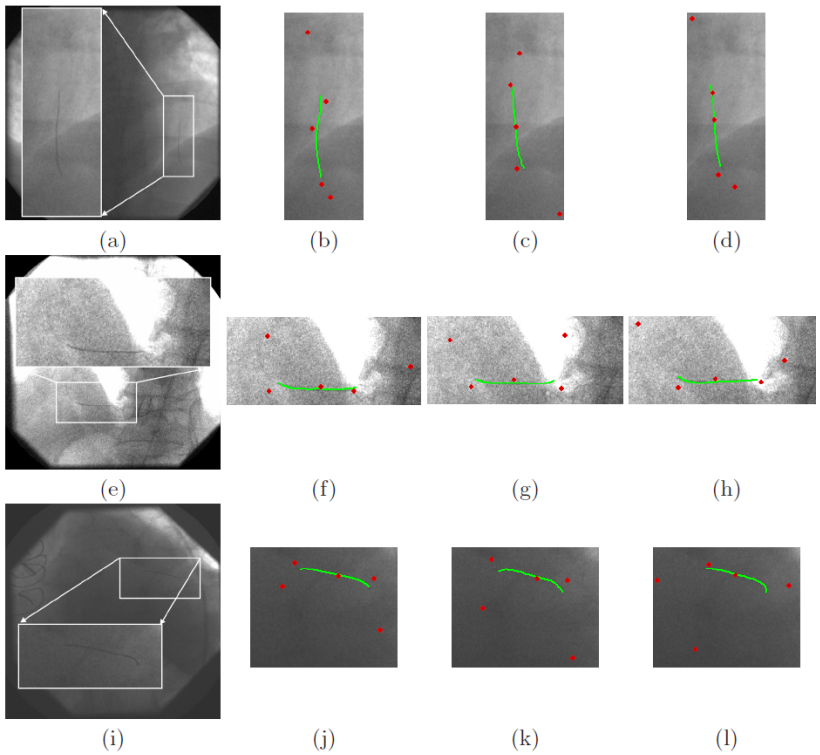

Figure 1.4. Results of the proposed guidewire tracking algorithm on three different endovascular videos. The original first image (left) and tracking result (right three images) for three consecutive frames are shown. In each frame the contour is overlaid on top of the original image [4].

XF is basically associated with strong doses of ionizing radiation to both patient and medical staff [36]. In addition, the toxicity of the contrast agents in XF has always

been an issue [37–39].

1.3. Ultrasonic tracking systems

UTS is one of the most popular alternatives for XF in addressing the issues discussed in 1.2. Although, ultrasonic image-guided tracking systems may suffer from a limited field-of-view there are techniques developed to extend FOV in real time imaging [40, 41].

To locate the tip of a catheter using sonomicrometry, an ultrasound piezoelectric transducer is mounted at the tip of catheter. Afterwards, the location of the transducer is found by measuring the time of flight of acoustic signals from the transducer at the tip to more than four other transducers acting as reference transducers. The time of flight of the acoustic signals between the reference transducers and the transducer at the tip of the catheter corresponds to the distance of the tip of the catheter to other reference transducers. In total, these distances provide an indication of the position of catheter in 3D frame determined by the positions of the reference transducers.

Figure 1.5 depicts a schematic diagram of a catheter inserted in a human body [5, 6]. Figure 1.6 shows the close-up of the inserted catheter [5]. The catheter (10) is shown disposed within artery (14) and conveyed thereby into the heart (5). Located on the head of the catheter (16) is a transducer (18). Located around the heart (5) and in the proximity of the catheter (10) are a number of of reference transducers 19.

A known catheter tracking system based on these sonomicrometric principles is described in [6]. This system measures the ultrasound travel times between pairs of transducers using short pulses of sound and clocked digital counters. The counters are started by the electrical pulse which drives the transmitting transducer, and are stopped by the detection of a pulse at the receiving transducer. Detection is accomplished by thresholding the received signal.

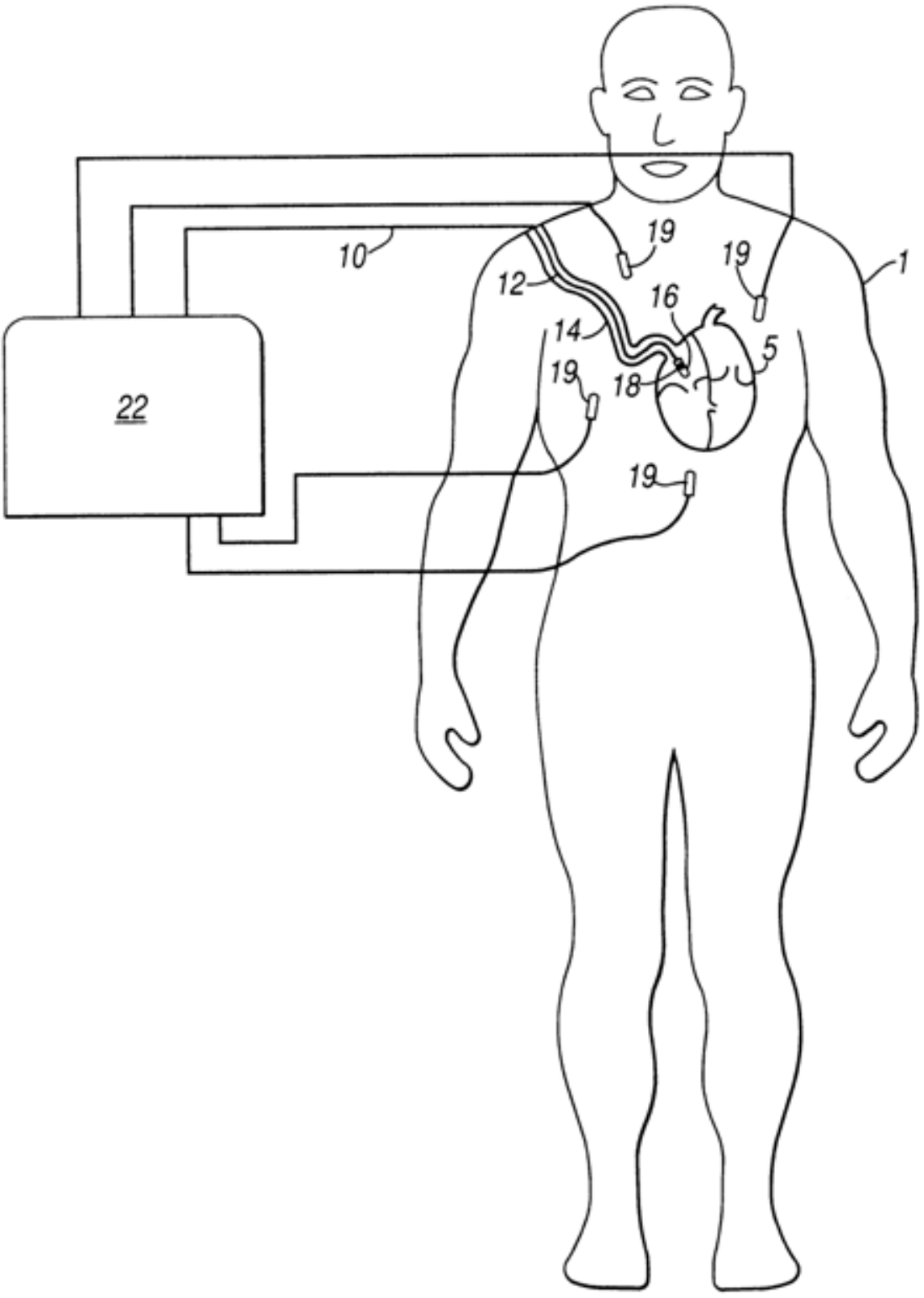

Figure 1.5. The schematic diagram of the catheter inserted in a human body. [5, 6].

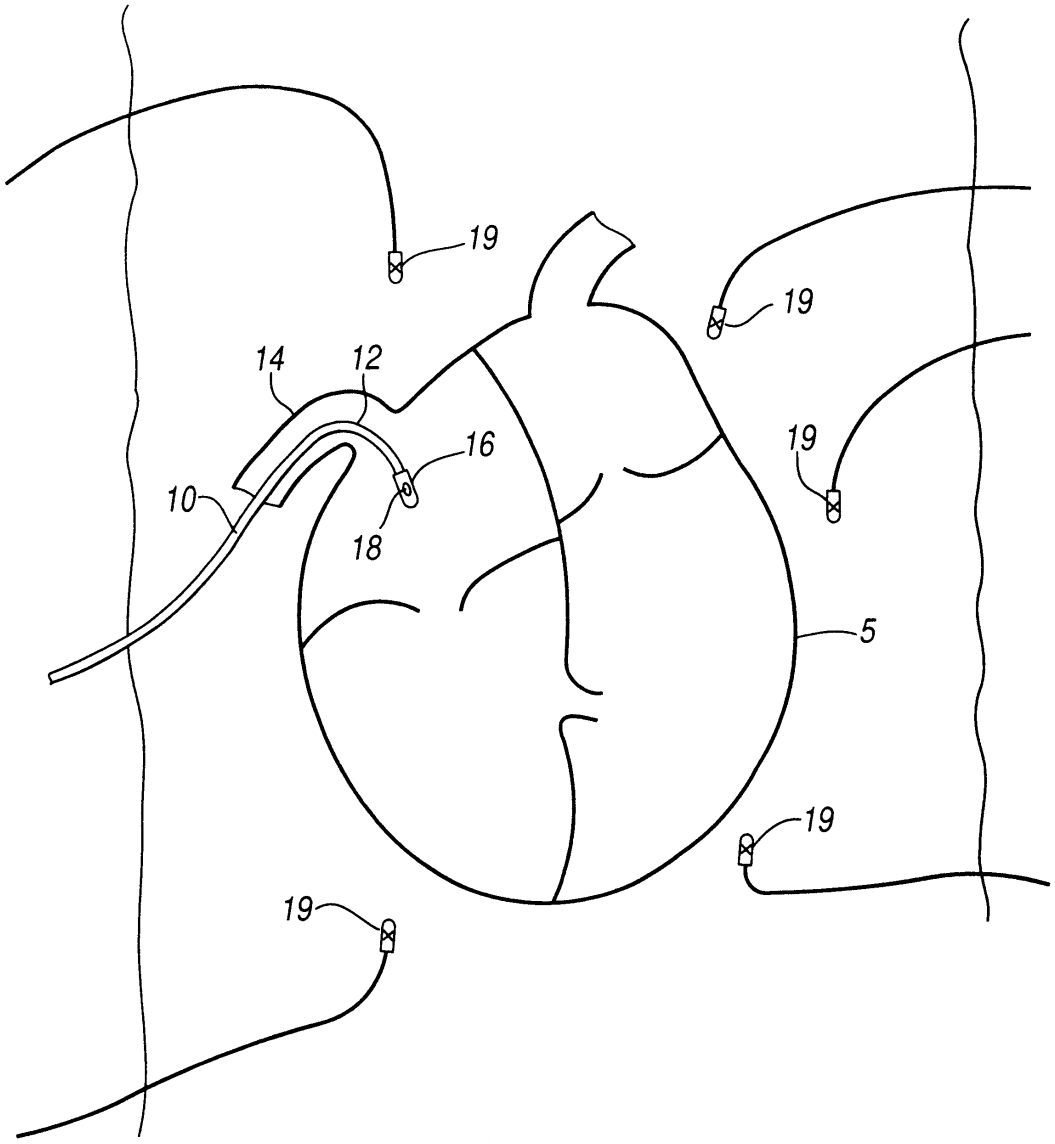

Figure 1.6. A typical catheter inserted through an artery into a heart, with reference ultrasonic transducers located around the heart, and in particular one transducer located on the head of the catheter inserted into the heart [5].

Each transmitting transducer is activated in turn, after waiting for the last transmitted pulse to arrive at all receiving transducers, and for stray reflections from the

various discontinuities inside the body to die away. By alternating the duty cycle between transmit and receive modes, the system can track and triangulate the three-dimensional positions for each transducer.

A disadvantage of this known catheter tracking system is that ultrasound signals do not travel in a straight line. Additionally, the speed of propagation of any acoustic wave is dependent on the material in which it is propagating. An acoustic wave travelling in the human body suffers from absorption, reflection, refraction, and scattering effects due to the material along its path. These non-idealities results in an error in determining the catheter location. An improvement in the accuracy of [6] is addressed by [42].

1.4. Electromagnetic tracking systems

EMTS are among the oldest technologies in motion capture traditionally used for animation in the entertainment industry. They can be either active or passive. Comparing to OTS, EMTS circumvent the limit of line-of-sight; however, it has generally low accuracy and a significant susceptibility to distortion from nearby metal sources. Early passive EMTS could get affected by neighboring metals quite extensively [43]; however, recent developments have placed EMTS in one of the most popular tracking systems in medical interventional operations. Recent technological improvements have enabled EMSTS much smaller sizes and more accurate sensitivity. Also, proper choices for metals can minimize the measurement error caused by eddy currents generated in the nearby metals [44].

Modern commercial products designed for medical applications are currently manufactured by Northern Digital, Ascension Technology, and Biosense Webster. All of these systems are active tracking systems, requiring wires between the sensor, typically placed at the tip of the catheter, and the tracking system, typically placed outside the human body.

One way to employ electromagnetic trackers is to externally generate a magnetic

field and track the tip of the catheter in real time by the help of an implanted sensor and comparing the electromagnetic space with previously acquired imaging space. This enables the monitoring of devices without the need of continuous imaging of the patient by conventional methods such as positron emission tomography (PET), XF, CT, and MRI. Figure 1.7 depicts the components and setup of an electromagnetic tracking system which relies on external magnetic field generator [45].

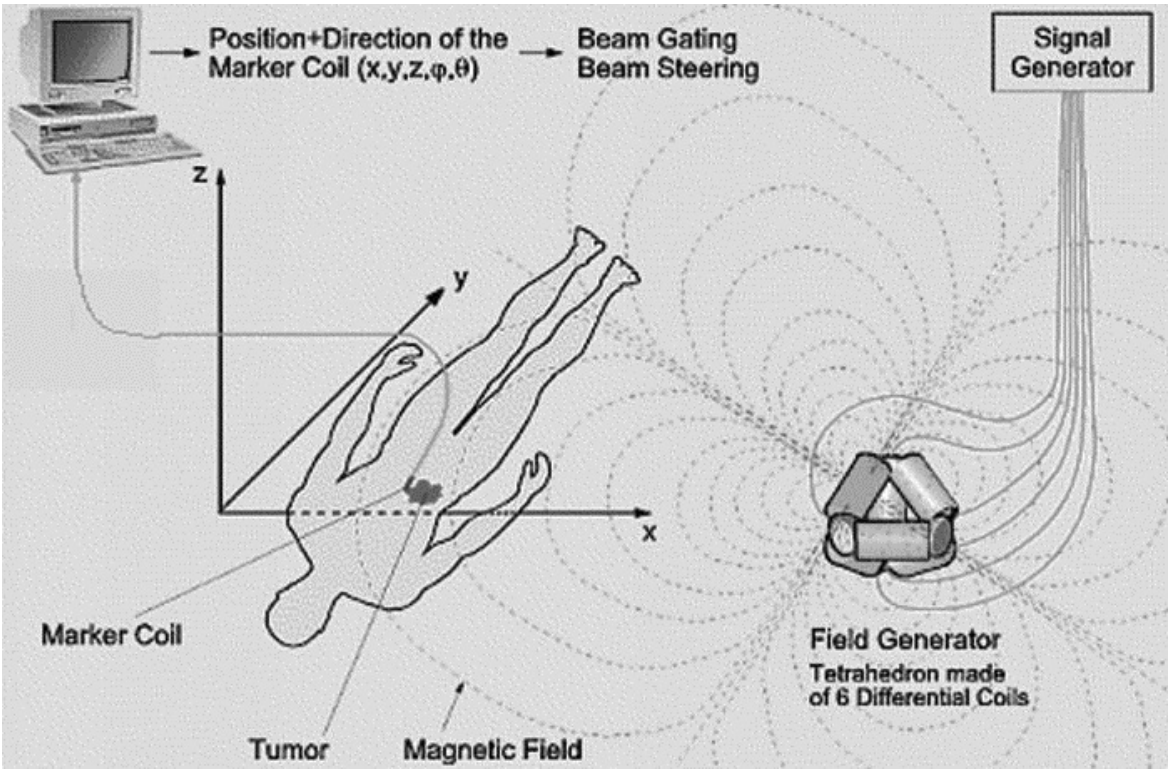

Figure 1.7. Electromagnetic tracking system set up and rationale (Reproduced with permission from Northern Digital Inc [7]).

Conventional types of EMTS utilize electric conductors for power and data transmission to the tracking unit at the tip of the catheter [46, 47]. Figure 1.8 shows the schematic diagram of a two-element capacitively coupled tracking coil that employs a fifty-ohm microcoaxial cable used to connect tracking coil to MRI receiver [8]. However, the strong radio frequency (RF) pulses in MRI generate an undesired level of heat in conductive materials which threatens the patient [48–52]. Although a number of techniques are employed to reduce the heat generation in interventional catheters

such as employing coaxial chokes [53] or exerting resonance frequency shift [54] fiber optic cables have always been a promising replacement for electric cables [55]. One major motivation of our main project is to eliminate these conductive transmission lines with fiber optic cables.

MRI an imaging technique which is being used vastly in clinical diagnosis, operational procedures, and research. The advantages of MRI are mostly due to its high contrast resolution comparing with ultrasound and tomography, computational simplicity in anatomical imaging and absence of ionizing radiation. The discussed advantages of MRI makes it a favorable technique for image-guided endovascular operations. However, localization of the catheter during the operation requires the utilization of other devices under MRI [56]. Among the major types of catheter-based interventional techniques under MRI, the use of EMTS can be very advantageous due to the presence of magnetic fields in MRI.

Table 1.1 shows a general comparison between the major image-guided tracking systems.

Table 1.1. A general comparison between the major image-guided tracking systems [12].

Tracking system	Pros	Cons
Optical tracking systems (OTS)	High accuracy, reliability	Line-of-sight limitation
Imag-based computational techniques	No need for external devices	Slow registration techniques, Poor image contrast
Ultrasonic tracking systems (UTS)	Ability to track flexible cathetrs, lack of line-of-sight limitation, Ease of imlementation,	Change of the speed of sound in different mediums, The multi-directionality of acoustic signals
Electromagnetic tracking systems (EMTS)	Ability to track flexible cathetrs, lack of line-of-sight limitation	Distortion due to nearby metals, low accuracy

1.4.1. An MRI compatible electromagnetic tracking system with MEMS RF resonators

Since this thesis works on the development of the MEMS sensor array used for the catheter localization system under MRI, the operation principles of MRI is needed to be shortly explained [57].

In MRI, an image is constructed by using the electromagnetic radiation, which is emitted by stimulated nuclear magnetic dipoles in the presence of an external magnetic field. There are many nucleus with non-zero magnetic moment that can be used for imaging,; however, since the Hydrogen (H) nuclei are numerous in human body and emit relatively strong signals they are chosen as the main material for imaging. In MRI environment, in the lack of external magnetic field the net magnetization of H dipoles is zero since their orientation is random. However, activation of a DC magnetic field aligns some of the H dipoles in the same direction as the magnetic field and precess them respectively. The frequency of precession is called Larmor Frequency (f_{Larmor}). Larmor frequency depends on the external field strength (B_0) and the gyromagnetic ratio of the nucleus (γ) as shown in Equation 1.1.

$$f_{\text{Larmor}} = \gamma B_0 \tag{1.1}$$

The value of gyromagnetic ratio (γ) for Hydrogen is 42.6 MHz/T. The alignment of H dipoles causes a nonzero magnetic moment (M_Z) parallel to the direction of the field (longitudinal direction). However, the net magnetization (M_{XY}) in the transverse direction (perpendicular to the external field) is still zero, because the phase of precession is random for every H dipole.

When H dipoles are excited by applying an RF pulse at their resonant frequency, which is equal to the Larmor frequency; some of them align against the external field and gain phase coherency. As a result of these, the net magnetization is flipped onto the transverse plane. While H dipoles return to their equilibrium state, M_{XY} decays due to dephasing. The emitted signal during this process is called free induction decay

(FID) signal, which is a decaying sinusoidal at Larmor frequency. The rate of decay depends on the type of the tissue.

In order to determine the position of the FID signal, gradient magnetic fields (B_{Grad}), whose strength is a function of the position, are added to the external DC magnetic field after the RF pulse is applied. Consequently, the frequencies of FID signals (f_{FID}) become dependent on the position as in Equation 1.2.

$$f_{\text{FID}}(x) = \gamma(B_0 + B_{\text{Grad}}(x)) \tag{1.2}$$

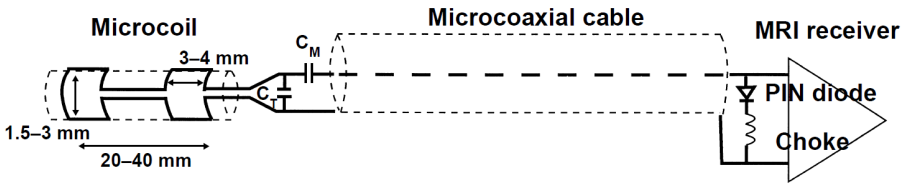

Figure 1.8. Schematic diagram of a two-element capacitively coupled tracking coil that employs a fifty-ohm microcoaxial cable used to connect tracking coil to MRI receiver [8].

Eventually, the frequency information can be mapped to the position in MRI. Our main project also utilizes this principle to find the position of the catheter.

MEMS technology in integration of optical systems has been actively utilized in lightwave communication for more than three decades [58]. Structurally speaking, MEMS is either used in mounting and/or packaging as done in [59] for vertical-cavity surface emitting laser (VCSEL) or utilized as movable apertures and reflectors for a variety of applications. As an optical switch, [60] presents a physical-parameter design of a 2D switch which is used for all-optical cross connects. Also, in [61] vertical torsion mirrors are utilized for free-space fiber-optic switches. Electrothermal MEMS actuators are used in variable optical attenuators by controlling the size of an aper-

ture formed by electrothermally movable blades [62] or moving the location of a pair of MEMS reflectors [63]. For optical bandpass filter realization a variable-aperture MEMS reflector is used in [64]. Magnetic actuation can also be used as done in [65] for a swing-type MEMS mirror which is used for a reconfigurable optical interconnect. On the other hand, optical read-out methods are also of a great use in detecting the deflection of MEMS cantilevers and resonators. For instance, [66] proposes an optical read-out method based on interferometers suitable for cantilever sensor arrays. The great potential of MEMS devices in integration of optical systems is one of the major motivations for the employment of RF MEMS sensor array enabling the optical signal transmission in our catheter tracking system.

The operating principle of the project, which encompasses this thesis work, can be summarized as follows: There is a microsystem at the tip of the catheter, which transfers the frequency information to the outside of the MRI machine via optical methods. Firstly, the FID signal around the tip is received and down-converted by an optically powered CMOS module [67]. Next, this CMOS module drives an RF MEMS module with the down-converted signal as an electrical current. After that, the RF MEMS module converts the electrical signal to a mechanical signal and optical readout is performed to measure the displacement of the resonator beam. This measurement transduces the signal from mechanical domain to optical domain and prepares the signal for transmission through fiber optic cable.

The task of optical transmission was given to an IR LED in previous stages of the tracking system development [67]. However, later on, the MEMS sensor array is preferred for its higher SNR, lower heat generation, and lower electrical power consumption. Also, the utilization of the DC magnetic field already present in MRI results in a low power solution for the whole catheter tracking system.

Figure 1.9 represents the whole tracking system showing the integration of fiber optic cables with the CMOS IC integrated with the MEMS sensor array (a family of individual resonators). The coil antenna is wrapped around the tip externally and receives the FID signals and provides input signal for the CMOS IC. The CMOS chip

is formed of a MR receiver which detects and downconverts the input FID signals and a photovoltaic cell that receives the optical power provided by the fiber optic cable and powers up the whole electronics. A resistor and a storage capacitor are kept as discrete components due to their large value requirements [67] and mounted at the back side of the substrate. The receiver drives the MEMS actuator with a pulse-width modulated (PWM) electrical current required for the actuation. Wire bonds provide electrical connection between the the CMOS IC and discrete elements. The optical fibers are mounted in parallel above the CMOS IC and the MEMS array. They are coupled to provide the optical power for the IC and align the readout laser on the MEMS sensor array.

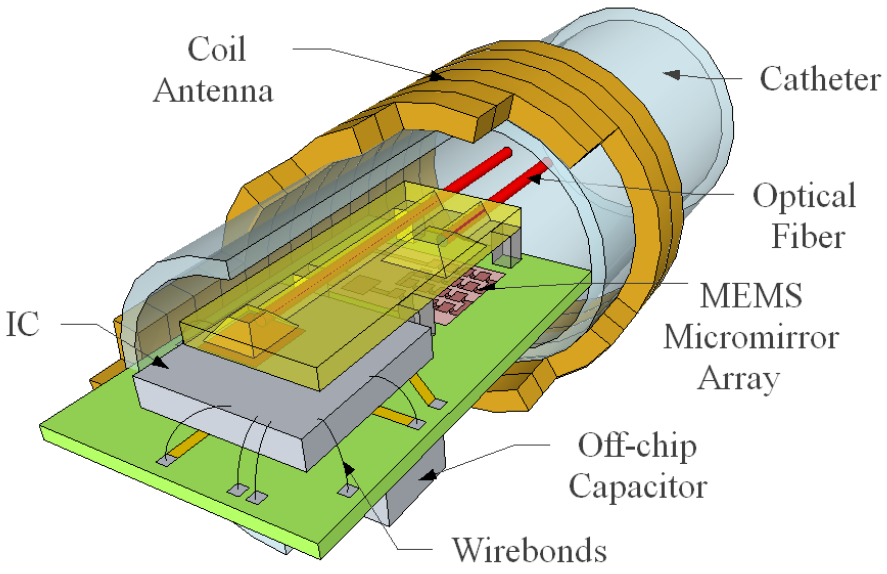

Figure 1.9. General representation of the tracking system.

The actuation mechanism of the MEMS resonators is based on the Lorentz force. When the current and the magnetic field are configured as shown in Figure 1.10 the mechanical force is induced in the out-of-plane direction [14]. The main advantage of using this method is that it allows us to utilize the strong DC magnetic field under MRI, which is either 1.5 T or 3 T for clinical-MRI, thereby resulting in a low-power solution. A small electrical current of 250 μA, can produce strong Lorentz force of 9 nN for a 121 μm-long bridge under 3 T external magnetic field according to Equation

1.3,

$$\vec{F_L} = \vec{i} l_r \times \vec{B_0} \tag{1.3}$$

where, $\vec{F_L}$ is the Lorentz force, $\vec{i}$ is the current, l_r is the length of the resonator, and $\vec{B_0}$ is the external field strength.

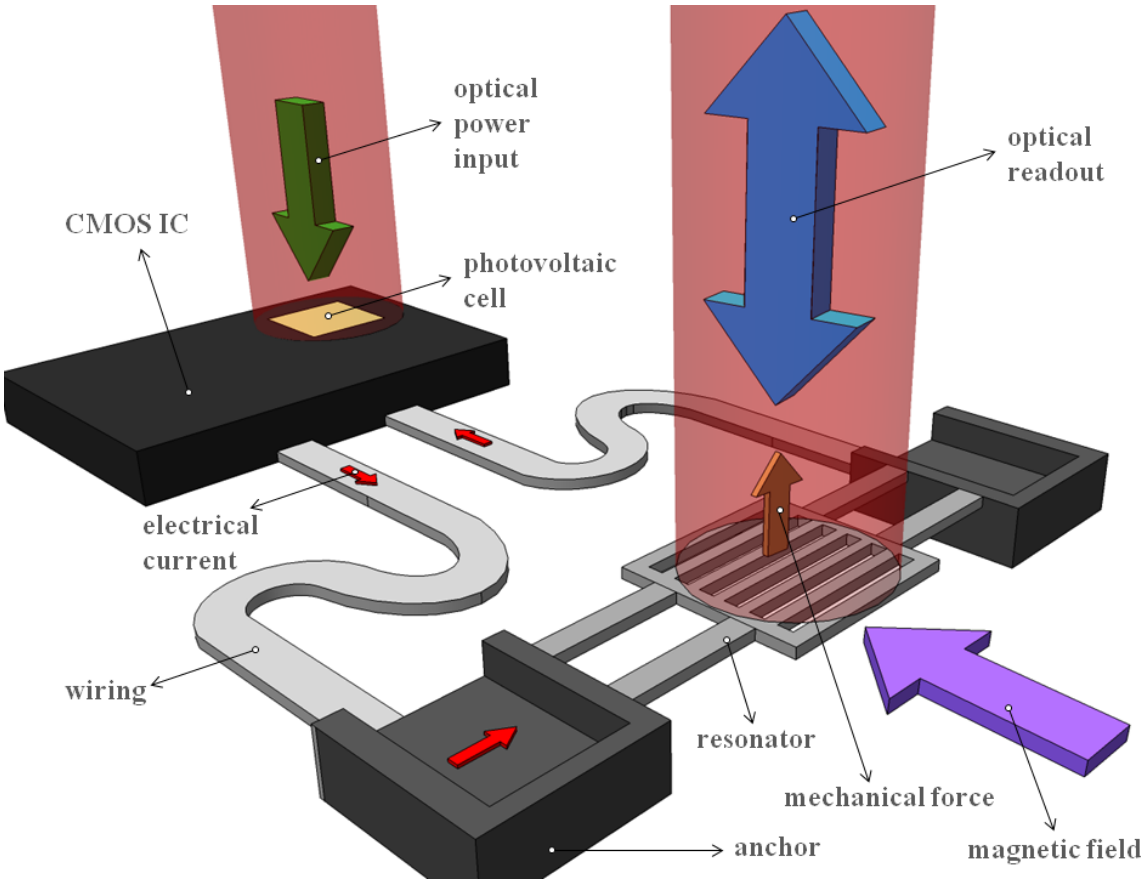

Figure 1.10. Representation of the MEMS resonator actuation mechanism and its integration with CMOS IC.

This thesis is focused on fabrication and characterization of MEMS transducers that are previously designed by [9]. The MEMS transducers are part of a complementary metal oxide semiconductor (CMOS)- based MRI catheter tracking system which is an EMTS which uses fiber optic cables for data and power transmission (TÜBİTAK-EEEAG 111E197).

The organization of this thesis is as follows: Chapter 2 discusses the structure and FEM simulation of the MEMS resonators. Chapter 3 explains the fabrication process step by step including failure scenarios. The characterization techniques and results are shown in Chapter 4 and, finally, Chapter 5 concludes the thesis and describes the future work.

2. DESIGN

Since LDV method can detect velocity of a mechanical structure in the direction of the reflected laser beam, our aim is to design resonators which have reflective surfaces that can move in the desired - in this case out of plane- direction. Although our different resonators have different geometry, the main idea is to have a clamped-clamped approach with a reflective mirror in between. Figure 2.1 shows an example of this type of resonators.

Note that the resonator has perforation holes in its mirror part. There are two reasons why we decided to put these holes. These are reducing the air damping effect and easing the removal of sacrificial photo-resist layer under the structure, which will be explained in detail in Chapter 3.

The design of the resonator which is used in this thesis is discussed in detail in [9]. The resonator is a clamped-clamped beam with either single or double flexures. At the center of the beam there is a mirror which is either diffraction grated or only patterned by square perforations. It is possible to detect the out-of-plane vibration by LDV for both types of mirrors. However, it is only for diffraction grated mirrors that is possible to detect the vibration by DGI. There are typically four types of devices (see Figure 2.2) that variance in dimensions lead to have totally 39 different devices with different resonance frequencies.

The geometrical parameters of a double flexure device with a diffraction grated mirror is shown in Figure 2.1. a stands for the width of a single grating and b stands for the gap between two gratings. mw stands for the width of the mirror and lm stands for the legth of the mirror. The flexure length is shown by lf, thickness is shown by t and the flexure width is shown by fw. The size of the diffraction grated mirror is typically 55×60 μm ($mw \times lm$) and the size of the mirror with square perforations is 40×40 μm ($mw \times lm$). Thickness of all the devices is 1.5 μm whereas the rest of the geometrical parameters vary from one resonator to another forming a family of 39 dif-

ferent resonators with different dimensions and different resonance frequencies. Table 2.1 shows the geometrical parameters of the 39 resonators. Typically, the decrease in length of flexure causes increase in resonance frequency. Also ,the higher the flexure width, the higher the resonance frequency. There are six beams that have diffraction grated mirrors with numbering of 5, 12, 13, 14, 15, and 16. The rest of the beams have mirrors with square perforations. The number of flexures is either one or two. The beams with one flexure are labeled as single and the beams with two flexures are labeled as double. The number of diffraction gratings vary between 8, 9, and 13. Also, the width of the gratings and the gap in between of the gratings varies between 2, 2.5, and 3. All these variations provide a range of neighboring resonance frequencies with a resolution of few kHz.

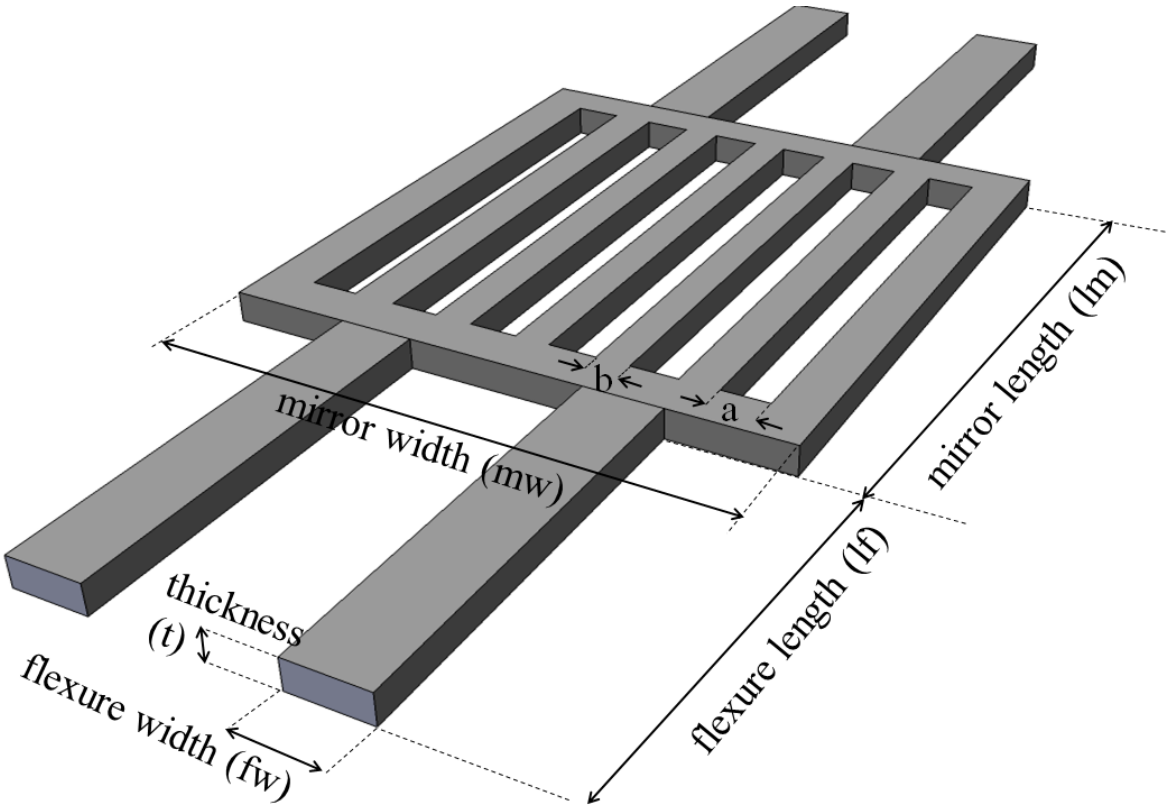

Figure 2.1. The geometrical parameters of a double flexure device with a diffraction grated mirror.

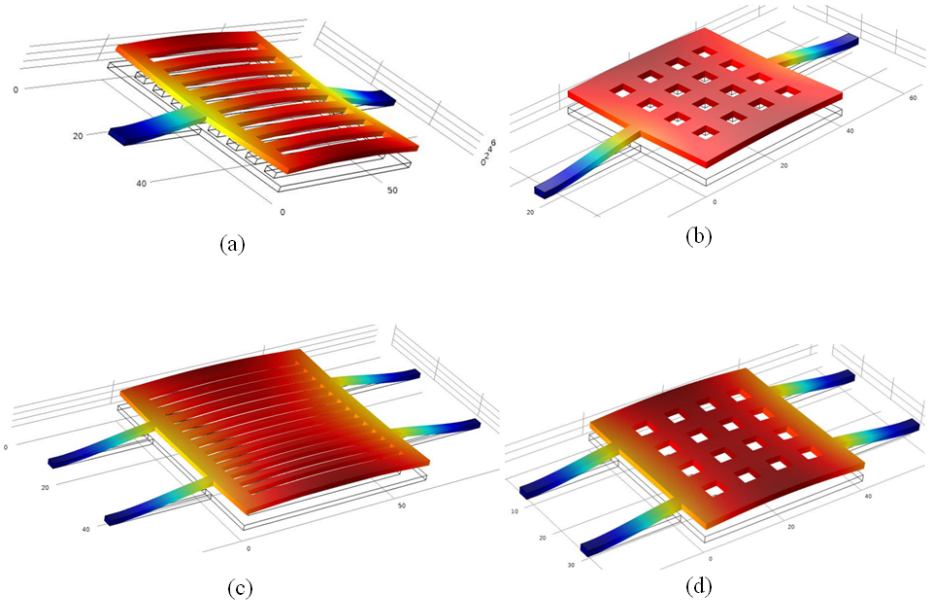

Figure 2.2. The four major types of resonators simulated in COMSOL Multiphysics. (a) Single flexure with diffraction gratings. (b) Single flexure with square perforations. (c) Double flexure with diffraction gratings. (d) Double flexure with square perforations.

It is not practical to detect high displacement throughout the whole frequency range of interest using only one resonator. Therefore we designed resonator families which have different resonators that are connected in series. Due to this series connection approach, all resonators are actuated by the driving signal at the same time. These resonators have different geometry, which leads to different resonance frequency values. These resonance peaks are distributed such that the measured displacement never drops below the minimum detectable level. By using an LDV spot which is big enough to cover all the resonators, we plan to detect strong signal for the whole

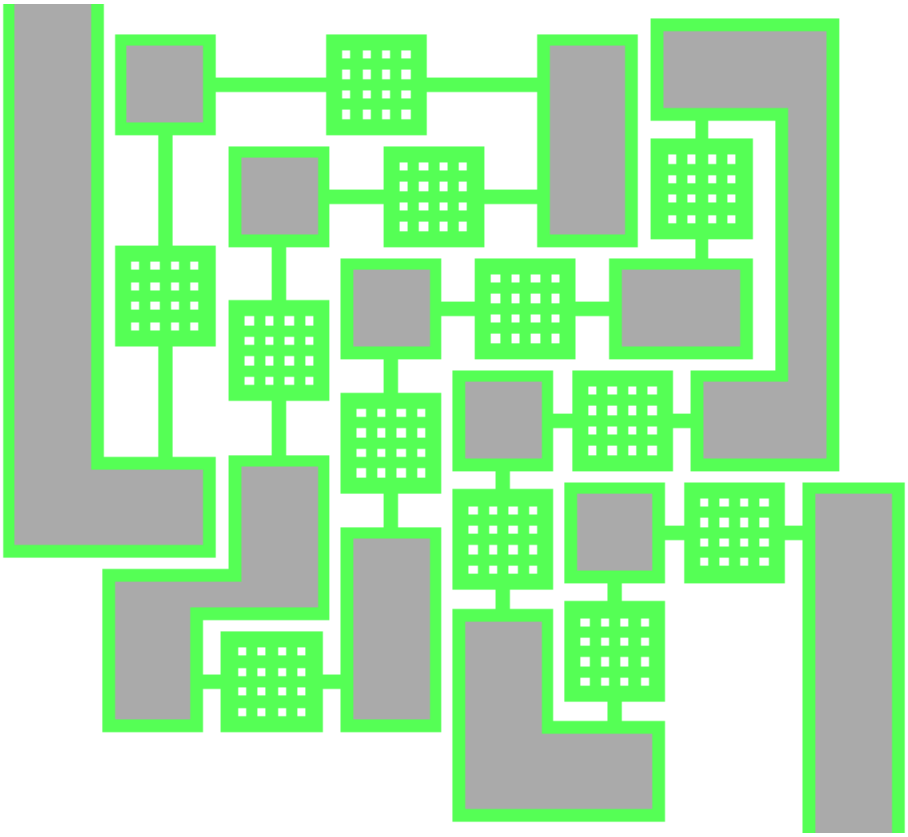

Figure 2.3. A micromirror resonator family [9]

frequency range. An example of such a family can be seen in Figure 2.3.

2.1. Theoretical background

This section explains the functionality of the out-of-plane displacement, spring constant, and resonance frequency for a clamped-clamped beam with a central mass (mirror). The 3D view of the resonator structure along with the necessary dimensions can be seen in Figure 2.1. Equation 2.1 shows the functionality of the displacement over a flexure [68].

$$w(x) = x^2(\frac{3(lf)}{2} - x)\frac{F_{eff}}{E(fw)t^3} \tag{2.1}$$

where F_{eff} is the total effective force, lf is the length of the beam's flexure, fw is the width of the beam's flexure, t is the thickness of the beam, and E is Young's Modulus. Figure 2.4 shows the profile of $w(x)$ with respect to x-axis. If we assume that the mirror does not bend while moving we substitute x with lf and obtain the displacement of the beam at the point that flexure meets the mirror.

$$w(lf) = \frac{(lf)^3 F_{eff}}{2E(lf)t^3} \tag{2.2}$$

Figure 2.4 shows the functionality of displacement with respect to x. The second order modeling of the resonator helps us to achieve the resonance frequency and spring constant of the resonator [69]. Ignoring the damping effect we have

$$M_{eff}\frac{d^2w(x)}{dx^2} + K_s w(x) = F \tag{2.3}$$

By static solution of 2.3 ($\frac{d^2w(x)}{dx^2} = 0$) we can obtain the spring constant K_s by considering the effective mechanical forces.

$$K_s = \frac{24E_x I_{yy}}{(lf)^3} \tag{2.4}$$

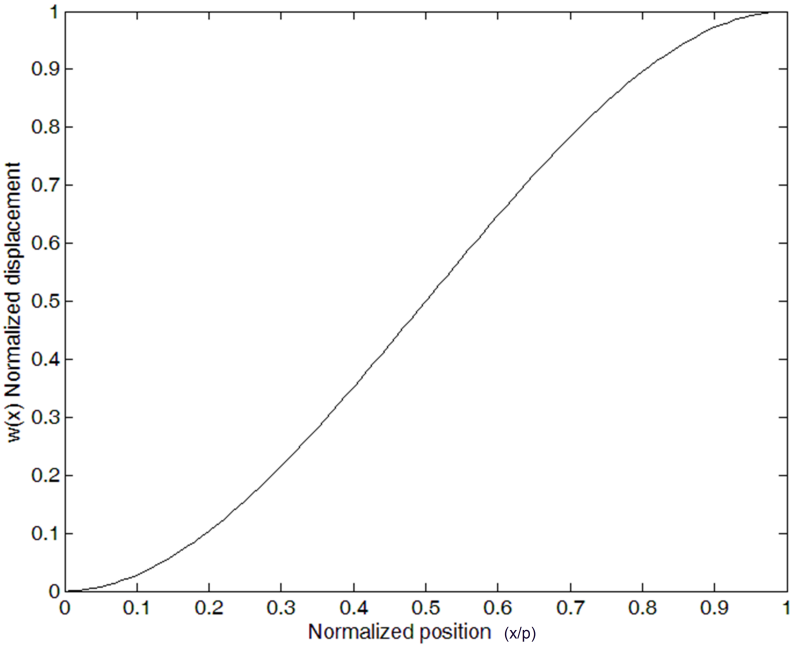

Figure 2.4. The profile of $w(x)$ with respect to x.

where E is Young's modulus and $Iyy = \frac{pt^3}{3}$ is the second moment of inertia with respect to the y-axis for the flexure cross-sectional area, and lf is the length of the flexure (coresponding to p in Figure **??**). The total mass is formed of the mass of the mirror and the mass of the flexures as shown in 2.5.

$$M_{eff} = M_m + \frac{26}{35} M_f \tag{2.5}$$

where M_m is the mirror mass and M_f is the mass of one flexure. Now, knowing the spring constant and the total mass we can obtain the resonance frequency

$$f = \frac{1}{2\pi} \sqrt{\frac{K_s}{M_{eff}}} \tag{2.6}$$

The resonance frequencies of all the resonators with different geometries are derived from mode analysis in 2.2.

2.2. Mode analysis FEM Simulations

There are six mode of resonance for each beam. Figure 2.5 shows the graphical illustration of mode analysis for a single flexure beam with square perforations (resonator number 17 from Table 2.5). However, the only modes that are detectable by the two desired optical methods (LDV and DGI) are out-of-plane sliding and rocking mode. Rocking mode frequencies are usually two times bigger than out-of-plane mode and it excludes them from the desired range of frequency response of the sensor array (see Table 2.1). Hence, the characterization is mostly focused on detecting out-of-plane resonance frequencies.

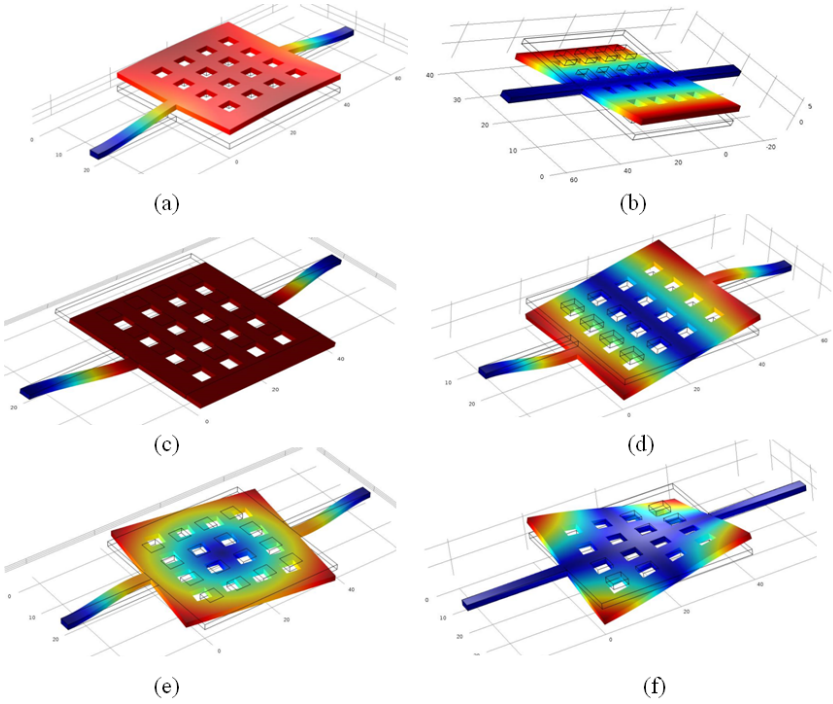

Figure 2.5. The six modes of resonance. (a) out-of-plane sliding. (b) torsional. (c) in-plane sliding. (d) rocking. (e) in-plane rocking. (f) sixth mode.

Table 2.2 shows the resonance frequency of six modes of motion for all 39 beams. According to FEM simulation results the out-of-plane resonance frequencies show the range of 145 kHz to 1.48 MHz whereas the rocking mode resonance frequencies start from 558 kHz until 4.33 MHz.

Table 2.1. The characteristics of all 39 beams

#	Flexure length (lf) (μm)	Flexure width (fw) (μm)	Mirror type	No. of flexures	No. of diffraction gratings	a (μm)	b (μm)
1	60	3	Square perforation	single	-	-	-
2	60	4	Square perforation	single	-	-	-
3	60	5	Square perforation	single	-	-	-
4	60	2.5	Square perforation	double	-	-	-
5	31	5	Diffraction grating	single	13	2	2
6	41	3	Square perforation	single	-	-	-
7	45	5	Square perforation	single	-	-	-
8	45	2.5	Square perforation	double	-	-	-
9	40	4	Square perforation	single	-	-	-
10	42	5	Square perforation	single	-	-	-
11	42	2.5	Square perforation	double	-	-	-
12	31	5	Diffraction grating	single	9	2.5	2.5
13	30	5	Diffraction grating	single	8	3	3
14	31	2.5	Diffraction grating	double	13	2	2
15	31	2.5	Diffraction grating	double	9	2.5	2.5
16	30	2.5	Diffraction grating	double	8	3	3
17	31	3	Square perforation	single	-	-	-
18	32	4	Square perforation	single	-	-	-
19	32	5	Square perforation	single	-	-	-
20	30	4	Square perforation	single	-	-	-
21	32	2.5	Square perforation	double	-	-	-
22	26	3	Square perforation	single	-	-	-
23	26	5	Square perforation	single	-	-	-
24	22	3	Square perforation	single	-	-	-
25	26	2.5	Square perforation	double	-	-	-
26	23	4	Square perforation	single	-	-	-
27	22	5	Square perforation	single	-	-	-
28	20	4	Square perforation	single	-	-	-
29	22	2.5	Square perforation	double	-	-	-
30	17	3	Square perforation	single	-	-	-
31	18	4	Square perforation	single	-	-	-
32	19	5	Square perforation	single	-	-	-
33	19	2.5	Square perforation	double	-	-	-
34	16	5	Square perforation	single	-	-	-
35	16	2.5	Square perforation	double	-	-	-
36	14	5	Square perforation	single	-	-	-
37	14	2.5	Square perforation	double	-	-	-
38	8	5	Square perforation	single	-	-	-
39	8	2.5	Square perforation	double	-	-	-

Table 2.2. The resonance frequencies of all 39 beams in six modes (kHz)

#	Out-of-plane sliding	Torsional	In-plane sliding	Rocking	In-plane rocking	Sixth mode
1	145.3314	259.4027	315.6028	558.5339	906.4583	-
2	162.0689	309.0468	472.7014	604.7998	1328.482	1705.417
3	175.5509	352.9947	642.1609	638.7496	1770.271	-
4	179.8541	345.6389	331.4438	650.0245	1656.175	-
5	230.6228	275.6028	1247.32	751.5695	-	1042.27
6	247.3701	312.805	562.6918	831.2691	1336.357	-
7	259.5519	405.215	984.7096	876.4871	2380.536	-
8	268.2511	435.0196	514.9958	904.6615	2252.977	-
9	280.4099	374.7867	863.895	925.1372	2002.231	2728.286
10	284.0719	419.1313	1088.857	941.2707	2550.575	-
11	294.2477	460.9167	571.6544	975.4965	2358.474	-
12	295.4036	280.684	1333.39	806.6927	-	1231.359
13	299.456	268.0261	1370.961	813.1645	-	1204.998
14	302.76	325.9562	692.3347	839.0237	1170.112	993.4972
15	318.372	387.9143	736.6966	887.0552	1350.585	1212.559
16	325.2901	379.2323	760.6488	909.9569	1335.875	1146.922
17	350.1807	355.6479	841.2231	1074.387	1756.648	2720.031
18	370.87	416.5154	1192.806	1146.5	2501.148	2748.431
19	398.5034	476.239	1604.281	1228.484	3334.676	2782.63
20	400.2823	428.3348	1305.564	1215.025	2662.869	2755.275
21	417.4727	585.0265	858.9821	1298.988	2687.231	-
22	431.8806	385.8103	1083.067	1261.978	2101.278	2733.262
23	505.752	524.3942	2132.888	1484.212	-	2812.044
24	520.6342	417.4381	1371.99	1463.839	2496.187	2748.558
25	535.2988	708.1773	1166.012	1601.155	2911.221	-
26	540.5338	487.1274	1891.14	1542.103	3475.081	2786.795
27	603.719	566.2739	2661.427	1712.919	-	2839.438
28	624.1549	513.5266	2282.462	1734.394	3993.708	2802.09
29	645.1921	828.1289	1485.481	1884.649	3106.152	4242.288
30	675.945	469.6288	1957.399	1817.702	3269.137	2775.84
31	691.0468	539.3952	2621.412	1887.74	-	2818.686
32	696.975	605.1348	3206.407	1928.125	-	2866.086
33	751.7567	949.5484	1828.656	2165.124	3298.726	4300.473
34	812.4118	648.8028	3956.553	2190.562	-	2898.216
35	886.9523	1109.271	2324.411	2532.643	3557.319	4350.921
36	905.8627	686.9474	4615.928	2403.883	-	2928.62
37	997.7527	1245.543	2788.365	2845.575	3785.687	4385.133
38	1288.923	865.0445	-	3223.61	-	3090.299
39	1480.039	1880.972	5644.026	4334.893	4981.23	4543.915

3. FABRICATION

The fabrication sequence of MEMS resonators is formed of six steps- two photolithography, sputtering the metallic seed layer, electroplating the structural layer, releasing, and etching. First of all, a photolithography is done to define the sacrificial layer. Anchors are the parts of the resonators that tighten the resonators to the substrate. The parts of the photo resist that are removed during the first photolithography define the anchors. After defining the anchor parts a thin layer of metal is deposited onto the whole wafer using a Vaksis Angora Sputtering System. This layer works as a seed layer for electroplating structural layer of the resonator. After the sputtering step, second photolithography is done to define the structural mask on top of the seed layer. The openings define the conductive areas that electroplating would take place. After the electroplating step is done for the desired thickness of resonators, oxygen plasma is used to release the devices by etching the sacrificial layer and the electroplating mask photo resist is remained. At the end, wet etching is used to etch the metallic seed layer from beneath the structural layer. Figure 3.1 presents the six steps of the fabrication in summary. Table 3.1 shows the final recipe for the fabrication.

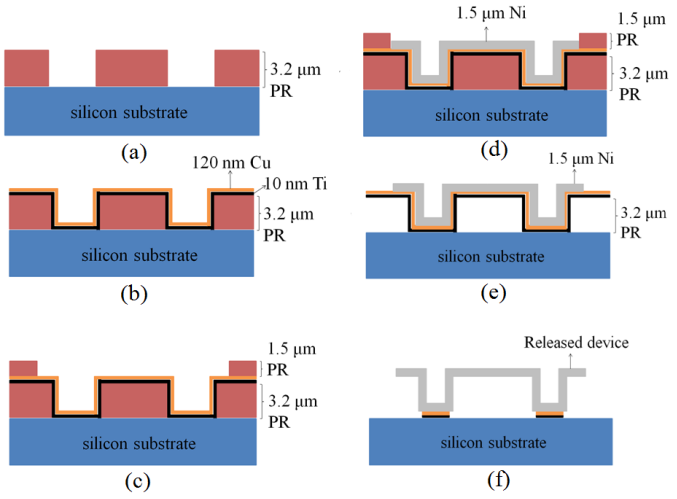

Figure 3.1. The six steps of fabrication shown from the side-view. (a) Photolithography 1 (b) Sputtering seed layer. (c) Photolithography 2. (d) Electroplating structural layer. (e) Releasing. (f) Wet etching.

3.1. Photolithography 1

In this section the definition of sacrificial layer (anchor mask) by PR is explained. The silicon substrate is coated with a layer of TI Prime to promote the adhesion of PR onto silicon. Then the PR is spin coated onto silicon. TI prime does not exert any additional thickness.

Figure 3.2a shows the anchor mask from top-view. The mask is a dark field mask which is followed by a positive PR. The red parts will be removed following the UV exposure and the rest of the wafer will stay covered with PR.

The thickness of the PR at this step had initially been chosen to be 1.4 μm. For thicknesses lower than 2 μm AZ5214E is used. The thickness of the PR at this step plus the thickness of the seed layer which is typically lower than 150 nm defines the gap between the resonator and the substrate. Experiments show that with gaps less than 2 μm the beams cannot be released and eventually stiction to the substrate happens. Accordingly, it is chosen to coat PR in thicknesses of more than 3 μm. For this range of thicknesses AZ4533 is used. A spin coating with a speed of 6000 rpm results in a thickness of 3.2 μm. This much of gap between the resonator and the substrate is proved to be good and chosen for the final recipe.

After coating the PR onto the silicon the soft bake is done for the evaporation of the solvent. The temperature of 110 Celsius degrees for 50 seconds is optimized. After the soft bake it is time for UV exposure. But before that, it is recommended to wait for about 10 minutes and let the PR absorb water molecules from the air. Eliminating the delay before the UV exposure may result in the appearance of bubbling and cracks during post processing.

The UV exposure is done with a dose of 100 $\frac{mJ}{cm^2}$. Then, the PR is developed for one and a half minute and photolithography 1 is finished. Before putting the sample into the sputtering machine for the next step it is required to hard bake the sample. This hard bake hardens the PR and evaporates the water and solvent from

the PR. For glass substrates it is recommended to hard bake at least 7 minutes at 120 Celsius degrees to prevent bubbling in post processing. However, for silicon substrates 3 minutes at 120 Celsius degrees is enough.

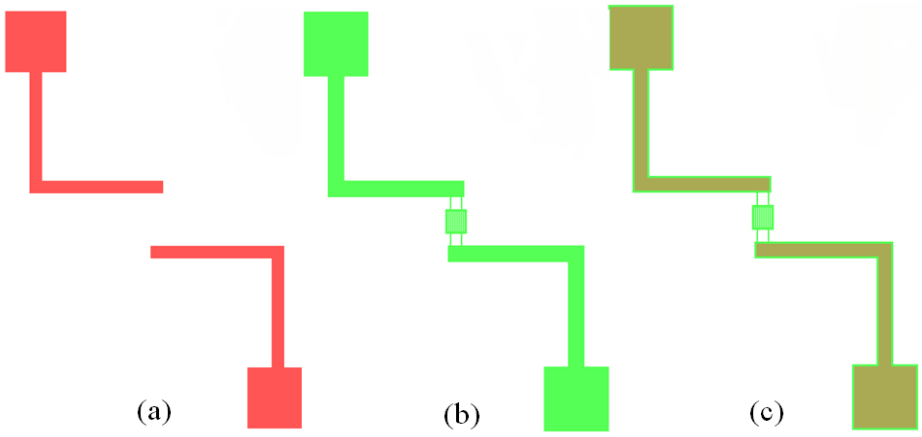

Figure 3.2. The two masks of the design from top-view for a double flexure diffraction grating resonator and their alignment on each other. (a) Anchor mask (b) Structural mask. (c) Alignment of the structural mask on the anchor mask.

3.2. Sputtering seed layer

The sputtering technique is chosen for deposition of the metallic seed layer. The type of material used for the seed layer is very critical to have a good electroplating later on. The important factors to be considered in choosing the proper material is discussed in Section 3.4.3.

Gold was initially chosen for the electroplating base (seed layer) and a thin layer of chromium for promoting the adhesion to the silicon substrate. However, the lack of nickel-compatible chromium and gold etchant at the time forced us to switch to copper as the seed layer and titanium as the adhesion promoting layer. Figure 3.1b shows the place of this step in the full sequence of fabrication process.

Many thicknesses of titanium and copper are tested to reach an optimum thickness of 10 nm titanium and 120 nm copper. One of the factors involved in optimizing

the thickness of titanium and copper is the appearance of cracks while baking the sample after sputtering. It happens due to the difference of the coefficient of thermal expansion (CTE) of the sputtered metals. Thin films are under either compressive or tensile stresses when deposited on the wafers. If the stress is due to the deposition technique it is called extrinsic stress. The difference of the CTE between two thin films on each other can result in buckling. This buckling is assumed to be the force which is exerted on the PR and results the cracks. Equation 3.1 shows the relation between the CTE of two thin films and the estimation of the coresponding extrinsic stress.

$$\sigma = \frac{E_t}{(1-\nu)}(\alpha_c - \alpha_t).\Delta T \tag{3.1}$$

where the indices c and t refer to copper and titanium, respectively, and E is the young's modulus of the titanium, ν is the Poisson ratio of titanium, α the CTE and Δ T the temperature difference.

In practice, decreasing the thickness of titanium and copper and/or the ratio of the thickness of titanium to the thickness of copper can decreases the number of the cracks. However, decreasing the thickness of titanium decreases the adhesion of devices to the silicon substrate and causes instability. Also, decreasing the thickness of copper decreases the electrical conductivity which is critical for having a good electroplating. Figure 3.3 shows the appearance of cracks while baking the sample during photolithography 2 after sputtering.

Figure 3.4 shows the placement of three glass substrates for the deposition of chromium and gold. Figure 3.5 shows the sputtering machine in the clean room.

Figure 3.3. The appearance of cracks in the PR while baking the sample after sputtering.

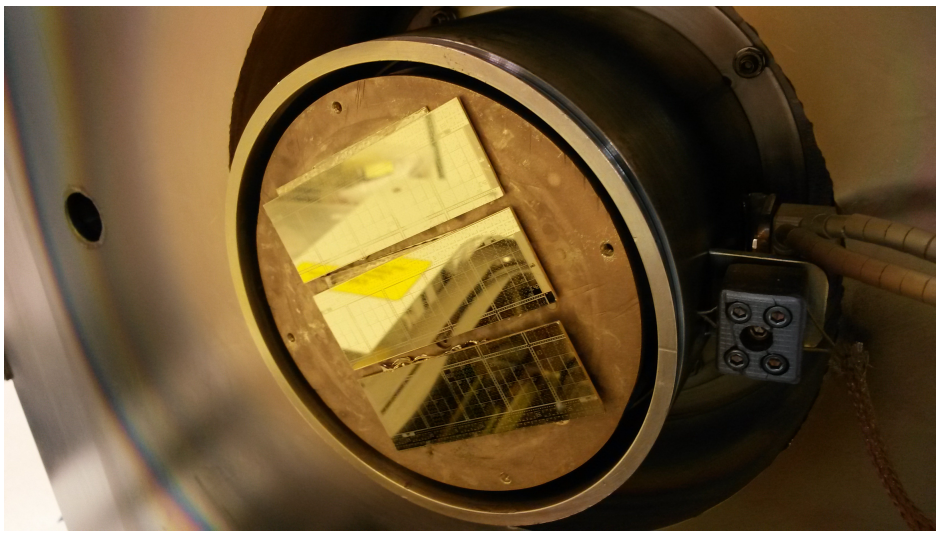

Figure 3.4. The placement of glass substrates into the sputtering chamber.

Figure 3.5. The VAKSIS ANGORA sputtering machine in the clean room.

3.3. Photolithography 2

This step is an image reversal lithography. The mask is clear field and the AZ5214E PR is normally positive. But it has the capability of image reversal to act like a negative PR. However, the image reversal does not work properly for thicknesses more than 1.5 μm and it prevents us to reach structural layers thicker than 1.5 μm . Figure 3.1c shows the place of this step in the full sequence of fabrication process.

Coating the sample with PR onto sputtered metal does not need any adhesion promoter due to the good adhesion of spin coated PR onto metals. The sample is PR coated with the speed of 6000 rpm resulting in a layer of 1.5 μm and soft baked at 110 Celsius degrees for 50 seconds. This is the step that if the hard bake before sputtering has not been enough and/or the thickness of the sputtered metals has not been chosen properly may cause cracks on the PR beneath the sputtered metal. These cracks decrease the conductivity of the sputtered copper such that usually makes the sample entirely useless.

After soft bake and a delay of 10 minutes the sample goes under the UV exposure. A masked exposure of 40 $\frac{mJ}{cm^2}$ is done. Now for letting the PR release the nitrogen

gas produced during the UV exposure it is necessary to have a delay of 10 minutes before the image reversal bake happens. Then, the sample is baked for 2 minutes at 120 Celsius degrees and gone under a flood exposure of 250 $\frac{mJ}{cm^2}$. Between the image reversal bake and the flood exposure a delay of 2 minutes is essential to let the sample cool down. After the flood exposure it is time for developing the sample for about one minute. This development time is critical since a few seconds of over development results in losing the diffraction grating definitions. On the other hand, the development may not clean the removing parts enough and it may result in partial low conductivity. The low conductivity of emerged metal areas after development is due to the residual thin layer of the PR after development. Since it is very difficult to find the optimum timing for development it is easier to slightly under develop the sample and then use the oxygen plasma to remove the residual thin layer of the PR. Typically, after 1 minute of development, putting the sample for three minutes in oxygen plasma at a power level of 200 is typically enough.

Now the sample is ready for electroplating. However, it is necessary to hard bake the sample for two minutes to harden the PR before immersing the sample into the electroplating bath. Figure 3.6 shows a micrograph from the sample which is ready for electroplating.

3.4. Electroplating

One of the major novelties of this thesis is the fabrication of miro-resonators by electroplating. It helps to achieve higher aspect ratios than depositing by sputtering. Lower residual stress and higher conformality are other advantages of electroplating over sputtering. Electroplating is a relatively easy and inexpensive way of depositing thin and thick films onto conductive substrates. A typical electroplating cell consists of an anode (Nickel target), cathode (conductive substrate to be plated), aqueous metal solution, and a power supply. When the power supply is switched on, the Ni ions are attracted to the negatively biased cathode. The Ni ions gain electrons at the cathode and are deposited on to the surface of the sample. The anode or the Nickel target is etched to produce ions for the electroplating solution and electrons

for the power supply. Hydrogen gas is released at the cathode during the reaction. This is undesirable since it lowers the plating efficiency and causes a poor quality electrodeposition.

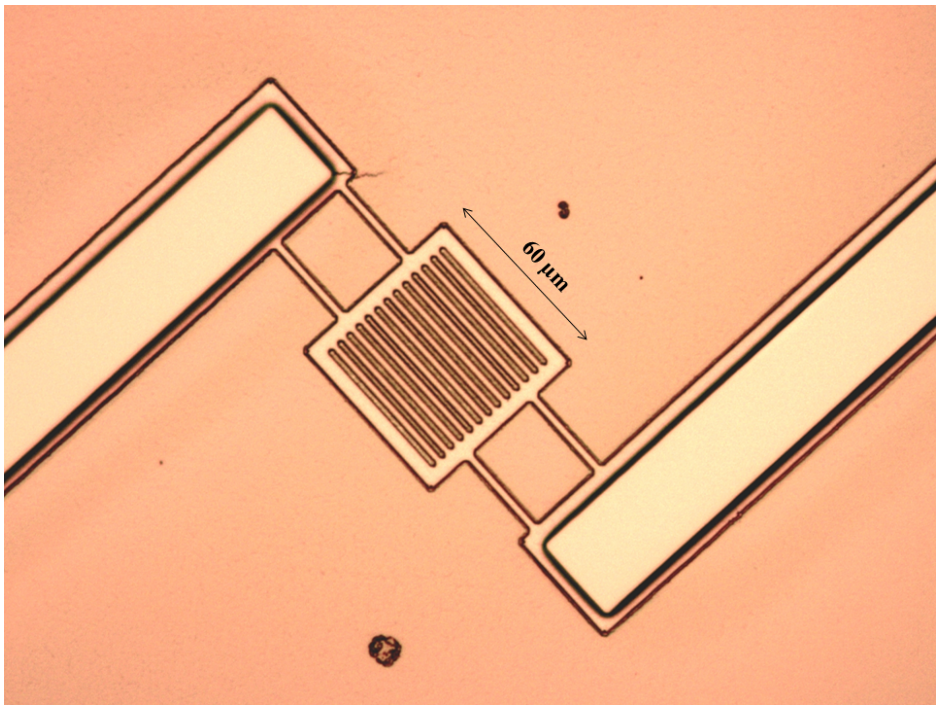

Figure 3.6. The top-view of the sample right after photolithography 2 and ready for electroplating.

The accumulation of hydrogen gas bubbles is minimized by constantly stirring the electroplating solution with the aid of a magnetic stir bar and stirrer [10]. Figure 3.7 shows the schematic of the electroplating process.

The amount of nickel deposited at the cathode and the amount dissolved at the anode are directly proportional to the product of the current and time and can be calculated from the expression

$$m = 1.095 \times aIt \tag{3.2}$$

where m is the amount of nickel deposited at the cathode in grams, I is the flowing current in the tank in amperes, t is the time that the current flows in hours, and a

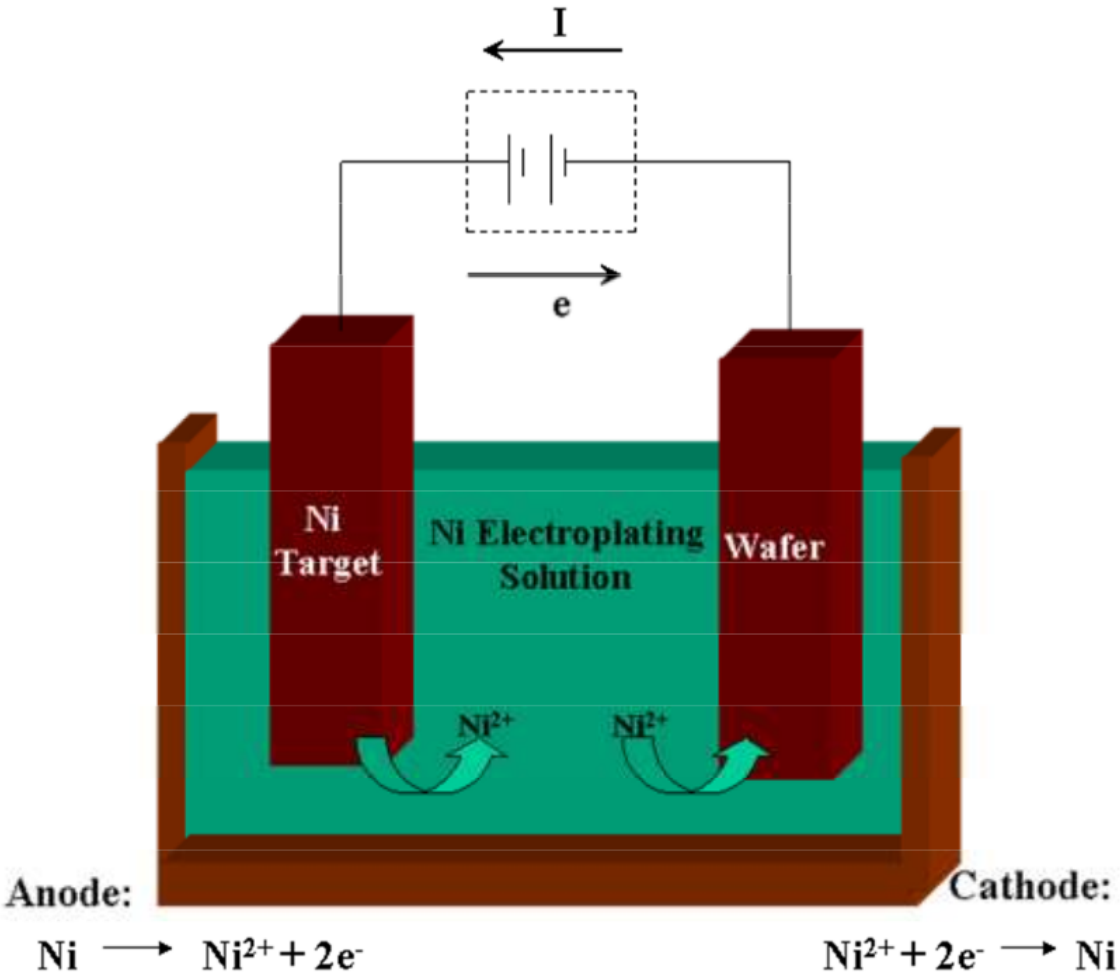

Figure 3.7. The electroplating bath schematics [10].

is the current efficiency ratio (see [70] for the definition of current efficiency). The parameters of our electroplating bath is explained in 3.4.5. Several kind of electroplating bath is available for nickel electroplating. One of the solutions that results in a very low stress thin film deposition is the sulfamate-based solution. In [11] the properties of electroplated nickel thin films have been investigated as a function of plating temperature and current density.

The commercial name of the electroplating bath used in this thesis is LECTRONIC 10-03 HSX. It is a sulfamate-based bath. Table 3.2 shows the composition as suggested by the producer company- Enthone. For the nickel source we have used a nickel ingot covered by two layers of filter.

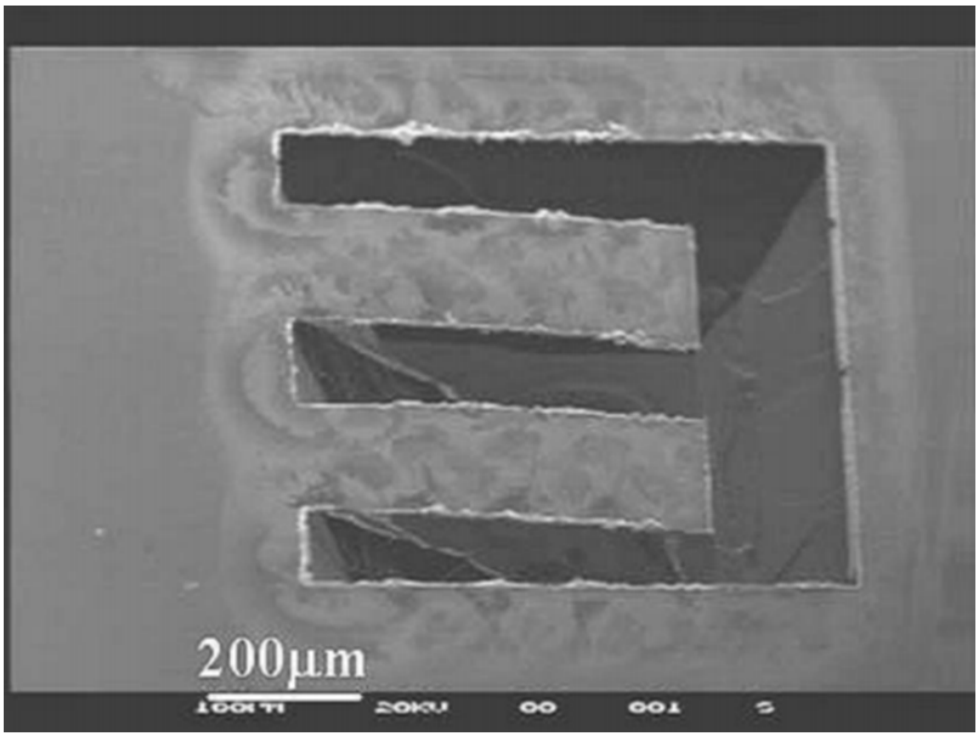

Figure 3.8. An SEM picture of a Ni cantilever made by laser micromachining [11].

A direct correlation between modulus of elasticity and the residual stress exists, which reveals that a material under high tensile stress may posses a low modulus of elasticity, and is not suitable for fabrication of MEMS devices.

The stress and resistivity of electroplated nickel onto copper is thoroughly investigated in [11] by characterizing nickel micro-cantilevers (see Figure 3.8). Figure 3.9 shows the functionality of Young's modulus, total stress, and resistivity to plating temperature, and current density [11].

Figure 3.10 shows the electroplating bath used in our project. It is formed of a tank and two capsules inside of it for covering the heater and the tempreture sensor. The current is supplied by a digital power supply and a controlling unit controls the temperature of the bath. The tank is placed on top of a magnetic stirring system for agitation.

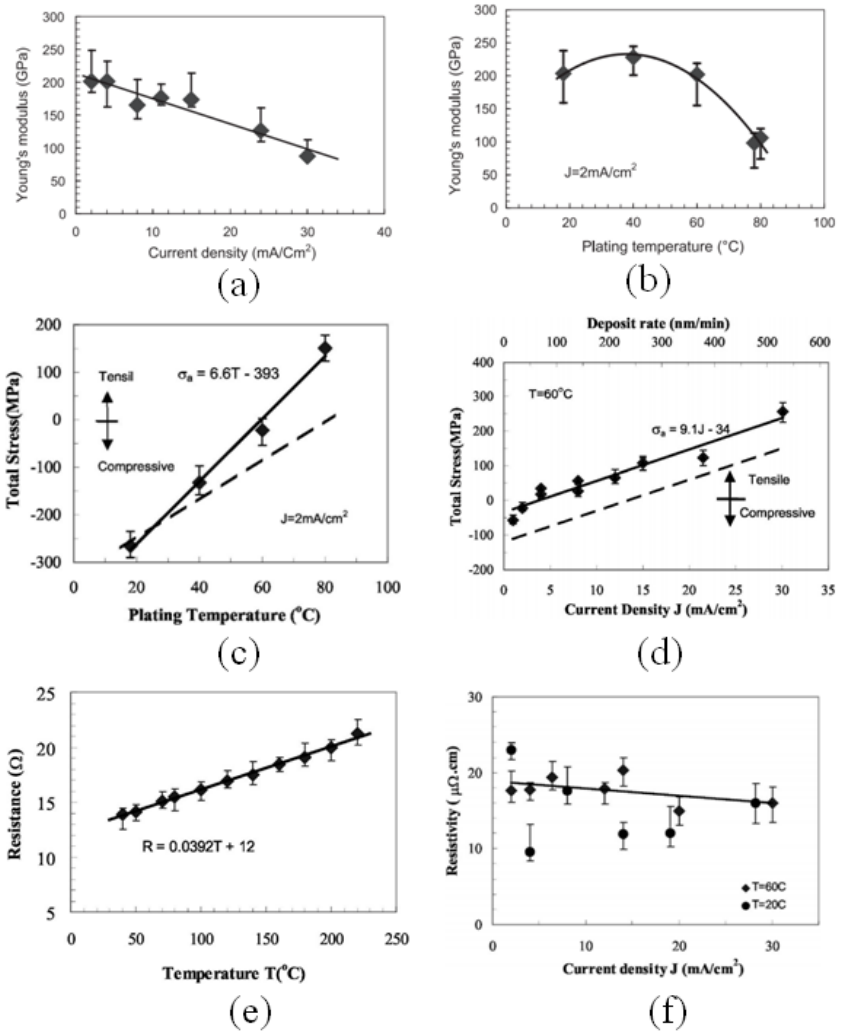

Figure 3.9. (a) Young's modulus as a function of plating current density plated at T=60 Celsius degrees (b) Young's modulus of Ni thin film as a function of the plating temperature, with J=2 $\frac{mA}{cm^2}$. (c) The dependence of the total stress on the plating temperature at a fixed current density of 2 $\frac{mA}{cm^2}$. The dashed line is the intrinsic stress after extracting the thermal tensile stress. (d) The dependence of the total stress on the plating current density at a fixed temperature of 60 C. Dashed line is the intrinsic residual stress after extracting the thermal stress. (e) Resistance as a function of measurement temperature for a Ni film plated at 12 $\frac{mA}{cm^2}$ and 60 Celsius degrees. It increases linearly with increasing temperature. (f) Resistivity as a function of plating current density. Although the data have a large scatter, it remains almost unchanged with plating current density [11].

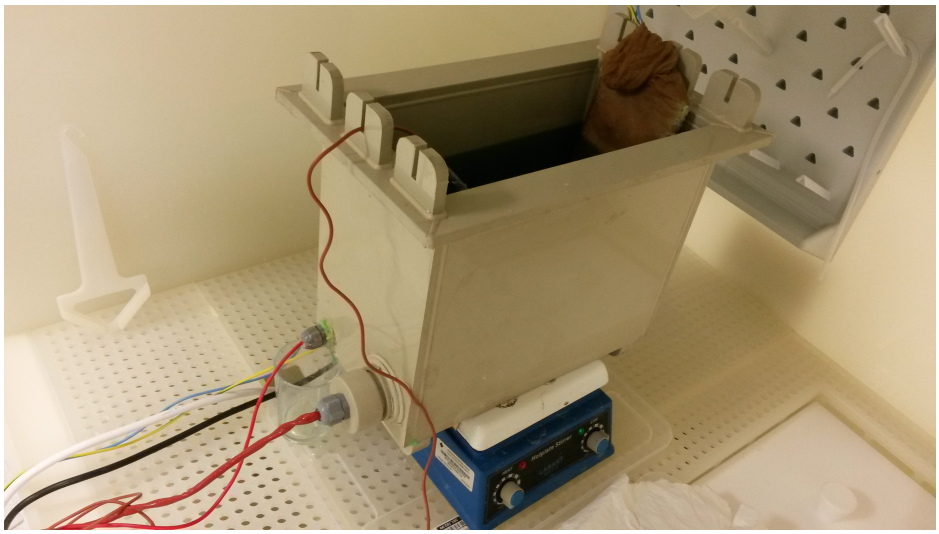

Figure 3.10. The electroplating bath in the clean room.

Current leakge into the substrate, while driving the resonators, is typically an issue for devices which are fabricated onto silicon substrate. Specially, if the substrate is a p-doped silicon wafer, as the one used in this project. Therefore glass substrate was initially suggested to eliminate the current leakage. However, we start our fabrication onto silicon substarte, because, we need to cut the circular wafer into small pieces for electroplating step (similar sizes to the samples shown in Figure 3.4). It would make the wiring and filtering (Figure 3.11) easier. Therefore, since it is more convenient to cut the silicon wafers rather than the glass wafers, it is decided to carry on with silicon substrates. Also, the adhesion of fabricated devices onto silicon substrates is better than glass substrates.

Although the current leakage is a potential risk during the operation of the resonators, the working point of the devices in our application (25 μA- RMS) does not cause the leakge current. Therefore, the utilization of glass substrate is skipped.

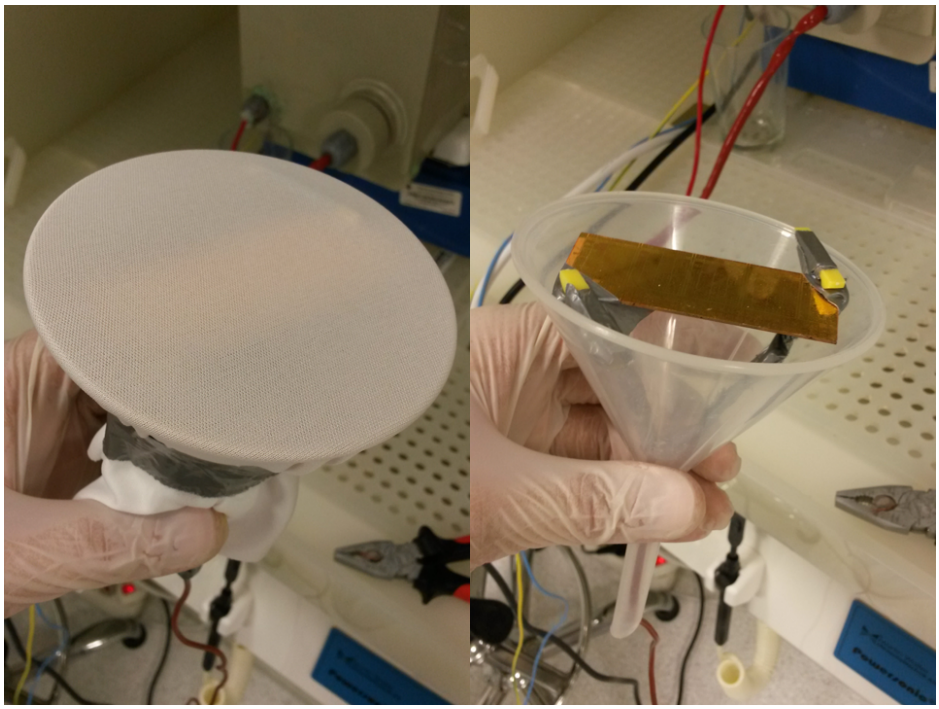

Figure 3.11. The filtering technique of the sample from the pollution in the electroplating bath.

Before coming up with the final recipe of electroplating many experiments are done which are useful to have them written in this section.

3.4.1. Electroplating nickel onto brass

Electroplating nickel onto brass wafers let us learn about the optimum range of electrical current density. It showed that a current density of more than 0.05 $\frac{A}{cm^2}$ can result in burnt areas in the corners. Stickers are used to cover the conductive areas that are not desired to get coated with nickel. Figure 3.12 shows the substrate before and after electroplating nickel onto brass. The specifications and results of electroplating onto brass is shown in Table 3.3.

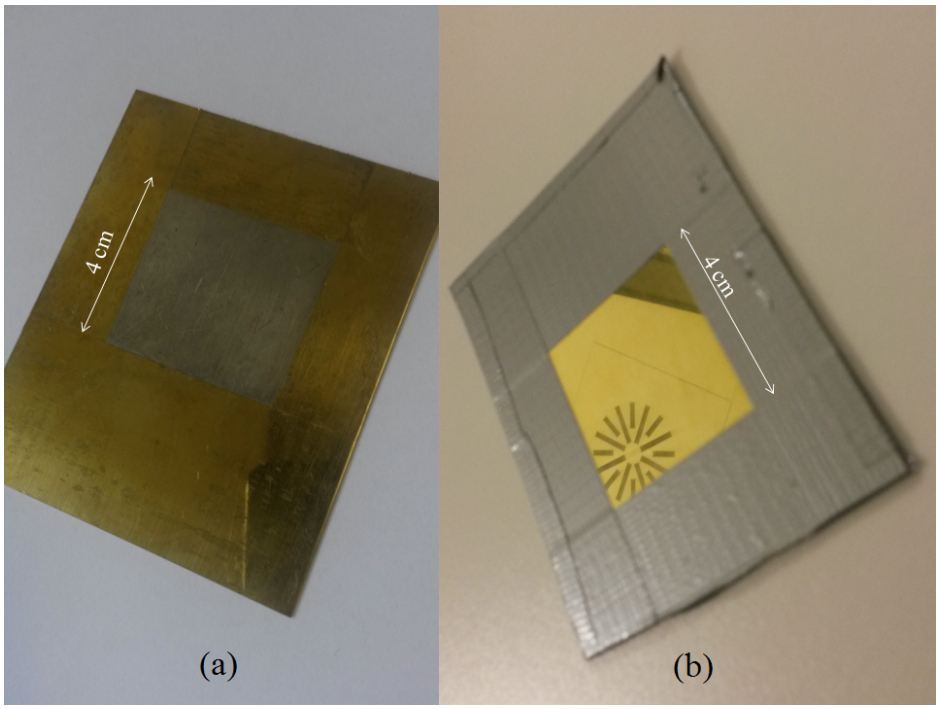

Figure 3.12. The substrate used for electroplating nickel onto brass. (a) after electroplating. (b) before electroplating.

3.4.2. Electroplating nickel onto PCB-copper

Then electroplating nickel onto PCB- copper is tested to find the time-thickness ratio with the current density of 0.01 $\frac{A}{cm^2}$. The electroplating onto PCB- copper substrate showed a linear relation between time and thickness. The average thickness of the electroplated nickel is calculated by measuring the weight of the sample before and after the electroplating. By substituting the value of nickel density, area of the electroplated nickel, and the differential weight of the sample the average thickness is calculated and written in Table 3.4. The rate of electroplating nickel of the electroplating bath with the current density of 0.01 $\frac{mA}{cm^2}$ is about 1 mg per minute.

Figure 3.13 shows the linear relation between time and thickness of electroplating nickel onto copper with an area of 6.25 cm^2 and current density of 0.01 $\frac{mA}{cm^2}$.

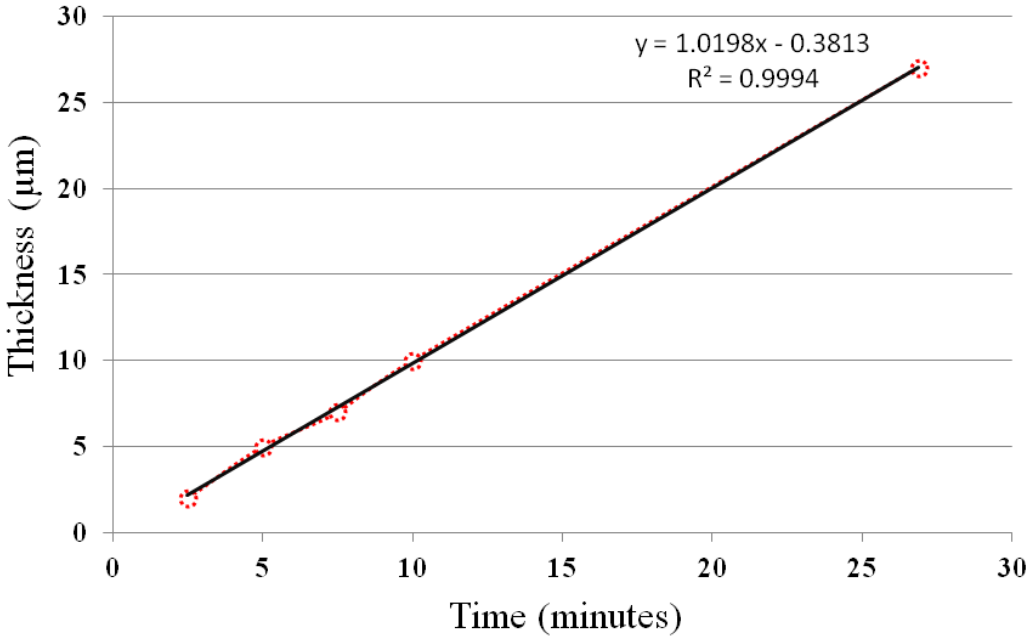

Figure 3.13. The relation between time duration of electroplating and the thickness of electroplated nickel onto copper for a sample with 6.25 cm^2 in area at a current density of 0.01 $\frac{mA}{cm^2}$.

3.4.3. Electroplating nickel onto sputtered chromium

It is not possible to electroplate nickel on every type of metal because elements and ions differ in the ease with which they are reduced or oxidized. In this section, electroplating nickel onto sputtered chromium is tested and failed. Two reasons are responsible for this failure.

First, the conductivity of chromium thin layer (200 nm) sputtered onto the glass substrate is turned out to be low. This is due to the oxidation of chromium which happens while exposed to the air. The thin layer of chromium oxide decreases the conductivity of the thin layer.

Second, which is the main reason of the failure in electroplating nickel onto chromium is the reduction potential of metals. Table 3.5 shows the activity series for metals. This activity series can be used to predict displacement reactions (see [71]). A metal will displace any metal below itself in the series [13]. Therefore, nickel ions are not able to displace chromium atoms and deposit themselves onto it.

Figure 3.14 shows the masked sample of sputtered chromium ready for immersing to the electroplating bath. The open area has area of 3.1 $cm2$. Desiring the current density of 0.01 $\frac{mA}{cm^2}$ it is calculated to have a current of 31 μA.

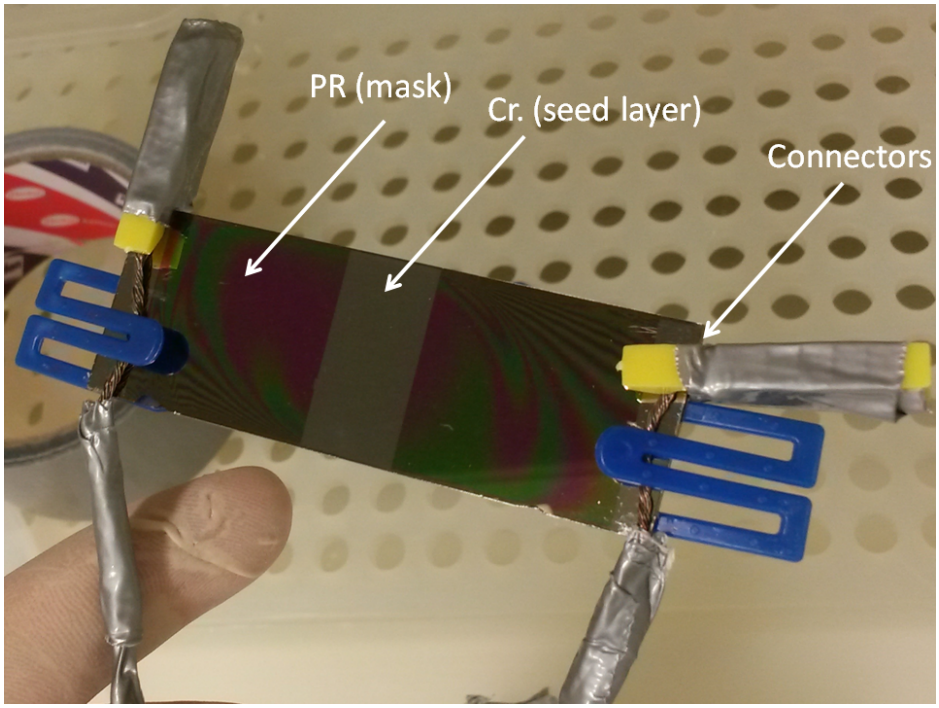

Figure 3.14. The masked sample of sputtered chromium ready for immersing to the electroplating bath.

3.4.4. Electroplating nickel onto sputtered gold

The electroplating nickel onto gold is tested successfully and devices are fabricated until the releasing step. However, the available gold etchant at the time attacked the nickel and ruined the structural layer. Figure 3.15 shows the fabricated devices after immersing to the Sigma-Aldrich standard gold etchant. It is clear how the struc-

tural layer is damaged. The adhesion promoting thin layer sputtered beneath the gold thin layer is initially chosen to be chromium. Later on, titanium is used. Though, they both showed a good performance as adhesion promoters.

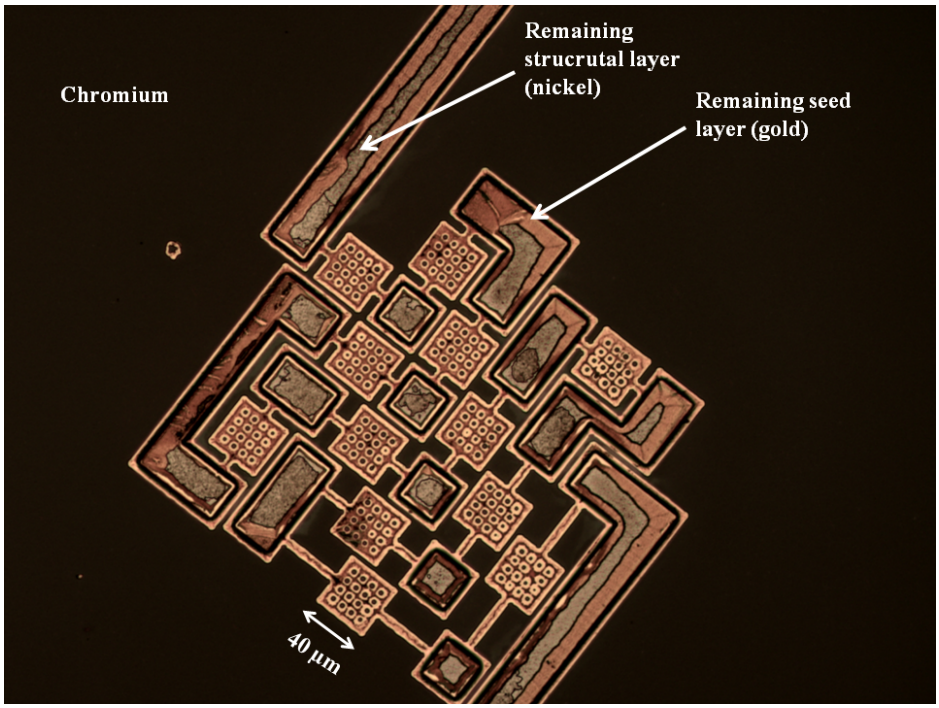

Figure 3.15. The damage to the structural layer exerted by nickel-incompatible Sigma-Aldrich standard gold etchant. Top-view of a maicrograph from the fabricated devices after immersion to the wet etchant.

3.4.5. Electroplating nickel onto sputtered copper

Copper is the final material used for the plating base. It is simple to produce its etchant from the available conventional acids, it is easy to deposit by sputtering, and it has a very good conductivity with thicknesses as low as 100 nm. Also, its electronegativity is close to the electronegativity of nickel and it makes it a very good electroplating base for nickel. As shown in Figure 3.13 the linearity of thickness with electroplating time is another parameter which makes copper an ideal choice for this application.

For the sputtered copper some experiments are done to find the relation of elec-

troplating time to electroplated nickel thickness. On average, at the current density of 0.01 $\frac{mA}{cm^2}$ each minute of electroplating deposits 100 nm of nickel. Therefore, a structural layer of 1.5 μm needs to stay in electroplating bath for about 15 minutes.

3.5. Releasing and wet etching

Once the structural layer is electroplated it is time for releasing. It can be done either by oxygen plasma etching system or by conventional Acetone and propanol. It is always preferable to avoid wet etching and use oxygen plasma for removing the sacrificial photo resist from the wafer. It is practiced and the results showed that a power level of 200 for about 10 minutes can indeed remove the photo resist remained from the both of lithography processes.

However, since a nickel-compatible titanium etchant are not available other techniques are required to remove the titanium residues on the wafer. Putting the sample in oxygen plasma for the removal of the first layer of photo resist (lithography 2) also attacks the sacrificial photo resist which is under the metallic seed layer. But, the residues of seed layers remain on the wafer (see Figure 3.16). Even wet etching the copper still do not remove the titanium residues on the wafer (see Figure 3.17). But, an immersion into acetone, propanol, and water for few minutes consequently by the help of simultaneous ultrasonic vibration, the titanium residues can be removed. Two micrographs from the released devices are shown in Figure 3.18 and 3.19.

Since the immersion into Acetone and propanol seems necessary for the lack of nickel-compatible titanium etchant the use of oxygen plasma for stripping off the photo resist can be evaded. It is due to capability of Acetone to quickly dissolve the photo resist. Therefore, eventually, the use of oxygen plasma for releasing the samples is eliminated from the final recipe of the fabrication process.

Figure 3.16. A micrograph from the top view after oxygen plasma and before etching copper. The sample is been inside the oxygen plasma for 30 minutes and the residues of copper and titanium are not removed.

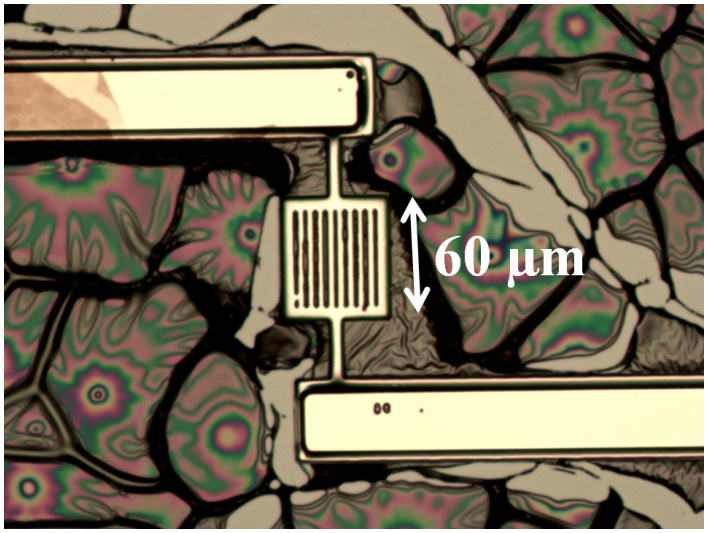

Figure 3.17. A micrograph from the top-view after oxygen plasma and etching copper. The residues of titanium are not removed.

The wet etchant used for copper is absolutely nickel-compatible. It is a 1:1:18 by volume glacial acetic acid : 30 percent hydrogen peroxide: deionized water. The etch rate is measured to be more than 500 nm per minute. Therefore, for the 120 nm thin layer of copper as few as five seconds is enough.

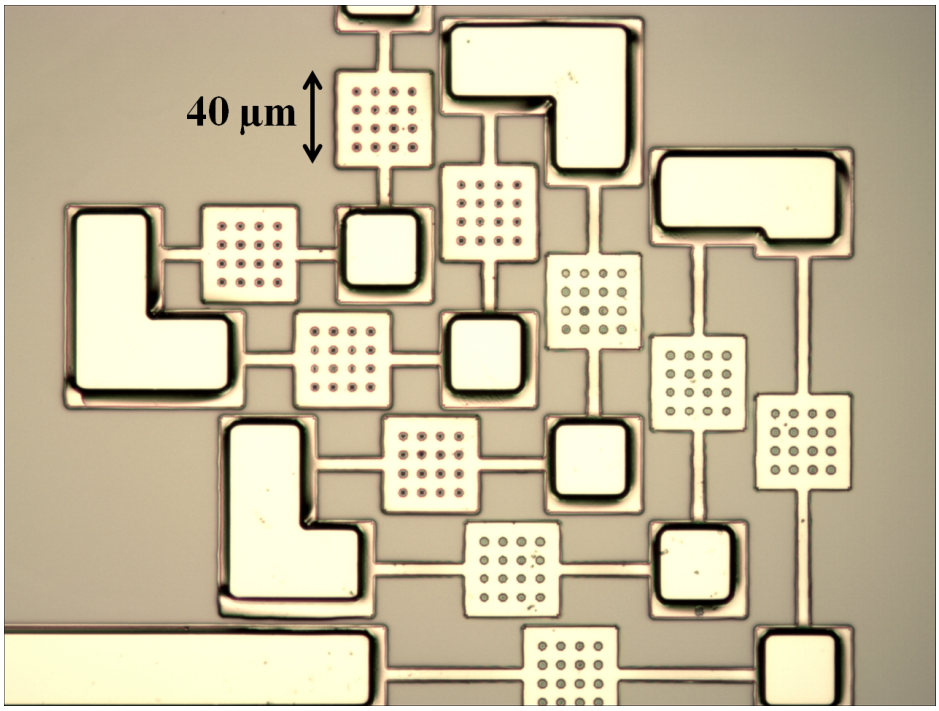

Figure 3.18. A micrograph from the top-view of a family of released resonators.

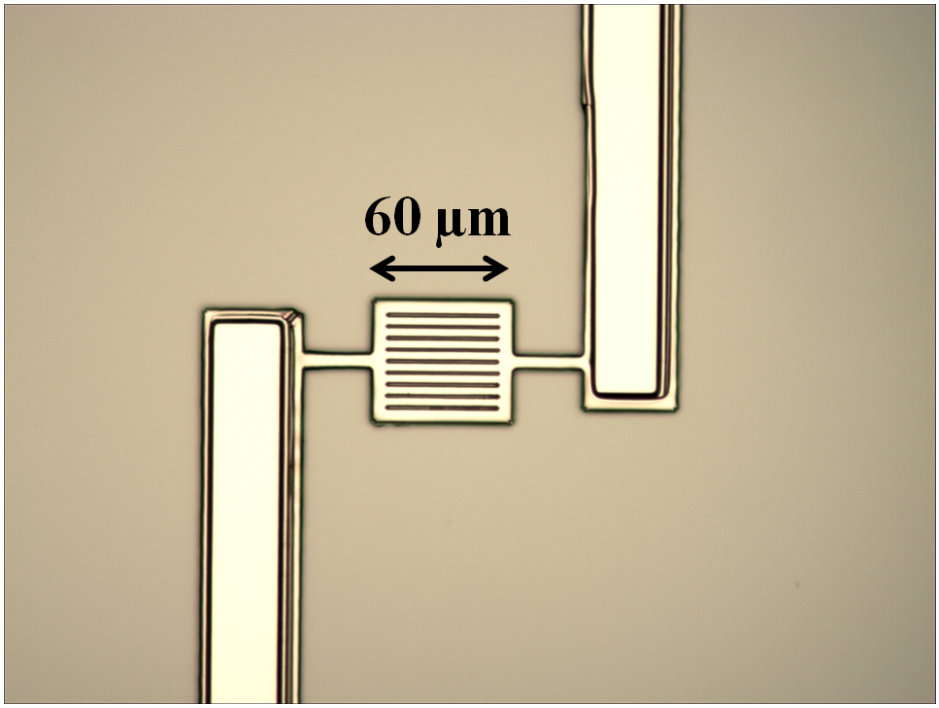

Figure 3.19. A micrograph from the top-view of a single diffraction grated released resonator.

Table 3.1. The fabrication recipe for the full sequence.

FIRST LITHOGRAPHY		AZ 4533
TI prime spin coating	4000 rpm	40 seconds
Baking	120 Celsius degrees	120 seconds
PR spin coating	6000 rpm	50 seconds
Soft baking	110 Celsius degrees	50 seconds
Delay		10 minutes
UV Masked Exposure	100 $\frac{mJ}{cm^2}$	soft contact
Development		90 seconds
Post Baking	120 Celsius degrees	180 seconds
SPUTTERING		Ti/Cu
Ti thickness	10 nm	
Cu thickness	120 nm	
SECOND LITHOGRAPHY		AZ 5214E
PR spin coating	6000 rpm	50 seconds
Soft baking	110 Celsius degrees	50 seconds
Delay		10 minutes
UV Masked Exposure	40 $\frac{mJ}{cm^2}$	hard contact
Delay		10 minutes
Image Reversal Baking	120 Celsius degrees	120 seconds
UV Flood Exposure	250 $\frac{mJ}{cm^2}$	soft contact
Development		60 seconds
Oxygen Plasma	Power= 200 Watts	180 seconds
Hard Bake	120 Celsius degrees	120 seconds
ELECTROPLATING		
Duration		10 minutes
Current Density		0.01 A/cm2
Wet releasing	Acetone & Propanol	2 minutes
Ultrasonic	Level= 3	3 minutes
Copper etchant		5 seconds

Table 3.2. Electroplating bath composition.

LECTRONIC 10-03 HSX	
Nickel as metal	113 $\frac{g}{l}$
Boric acid	40 $\frac{g}{l}$
Lectronic 10-03 Anode Activator	85 $\frac{ml}{l}$
Lectronic 10-03 HSX adition agent	22 $\frac{ml}{l}$
Lectronic 10-03 wetting agent	10 $\frac{ml}{l}$
PH	3.5
Tempreture	58 degrees of Celsius

Table 3.3. The specifications and results of electroplating nickel onto brass.

Curent Density (J)	0.01 $\frac{A}{cm^2}$
Area	16 cm^2
Current	160 mA
t= 5 min	Average Thickness= 0.56 μm
t= 10 min	Average Thickness= 1.82 μm

Table 3.4. The specifications and results of electroplating nickel onto PCB- copper.

Curent Density (J)	0.01 $\frac{A}{cm^2}$	
Area	6.25 cm^2	
Current	62.5 mA	
t= 10 min	Average Thickness= 1.80 μm	Plated Nickel Weight= 10 mg
t= 7.5 min	Average Thickness= 1.25 μm	Plated Nickel Weight= 7 mg
t= 5 min	Average Thickness= 0.9 μm	Plated Nickel Weight= 5 mg
t= 2.5 min	Average Thickness= 0.36 μm	Plated Nickel Weight= 2 mg
t= 26.88 min	Average Thickness= 5 μm	Plated Nickel Weight= 27 mg

Table 3.5. Activity series for metals [13].

No.	**Metals**
1	lithium
2	potassium
3	calcium
4	sodium
5	magnesium
6	aluminum
7	zinc
8	chromium
9	iron
10	nickel
11	tin
12	lead
13	hydrogen
14	copper
15	mercury
16	silver
17	platinum
18	gold

4. CHARACTERIZATION

The frequency response of the fabricated devices is characterized under an external magnetic field generated by permanent magnets. Generation of a magnetic field as strong as 3 Tesla similar to the MRI environment is not possible in the laboratory. Therefore, two cubic permanent magnets (N48) with a residual flux density of about 14 KGs are chosen based on their availability, size, price, material, and strength (see Figure 4.1).

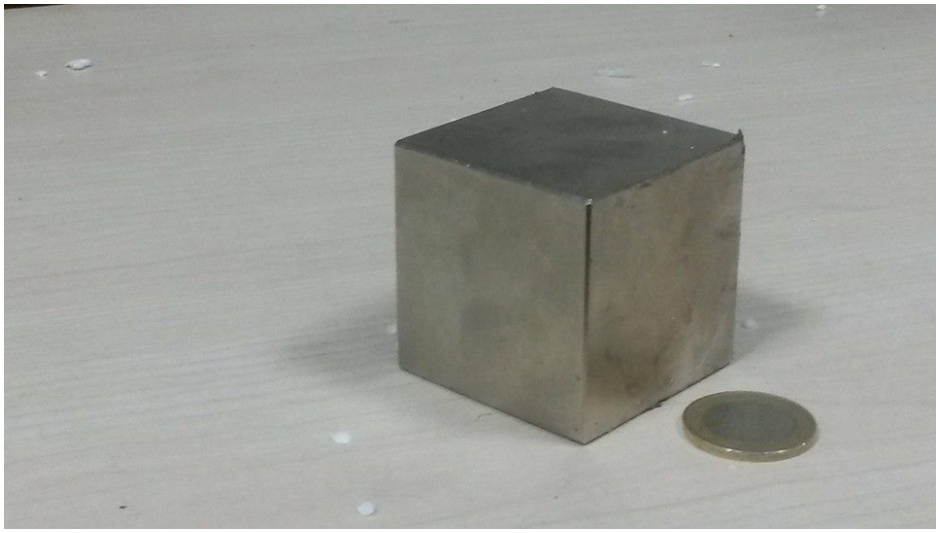

Figure 4.1. The comparison of the size of magnet with a 1 Turkish Lira coin.

The holder of the magnets with 1 inch gap in between is designed for the placement of the MEMS resonator and manufactured by stereolithography. The gap is designed such that the resonator would be placed perpendicular to the magnets and an almost uniform magnetic field would pass perpendicular to the resonator (see Figure 1.10 for the resonator configuration with respect to the magnetic field and LDV). Figure 4.2 shows the schematics of the configuration of magnets and the resonator.

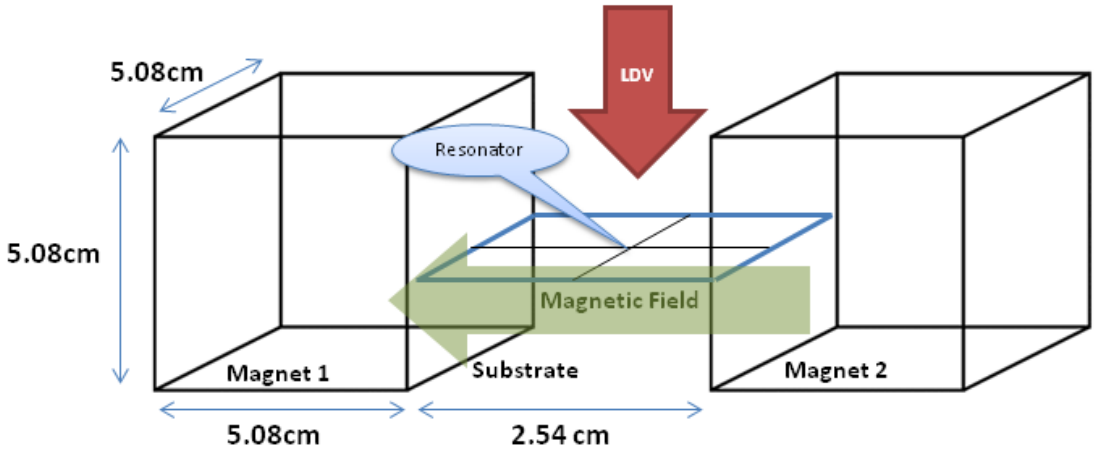

Figure 4.2. The schematics of the configuration of magnets and the resonator.

The magnetic field in the central axis of the gap and between the magnets is measured by a gaussmeter to be 0.62 Tesla at the center of the central axis (0.5 inches from each magnet). It is almost five times smaller than MRI which can be compensated by increasing the nominal driving electrical current of the resonator to reach a mechanical force comparable to what is present under MRI.

Figure 4.3 shows the implemented setup with magnet holders having the sample in between mounted on a 3D stage, the probe stations and the laser beams.

The green laser is for observing the tip of the probes to probe down the device. It works like a microscope. The reflection of the green laser let the operator to see a magnified view of the spot with showing the tips of the probes and the resonator which is under characterization. It is needed to put a white surface in front of the reflected beam to see the reflected image of the resonator and the tip of the probes.

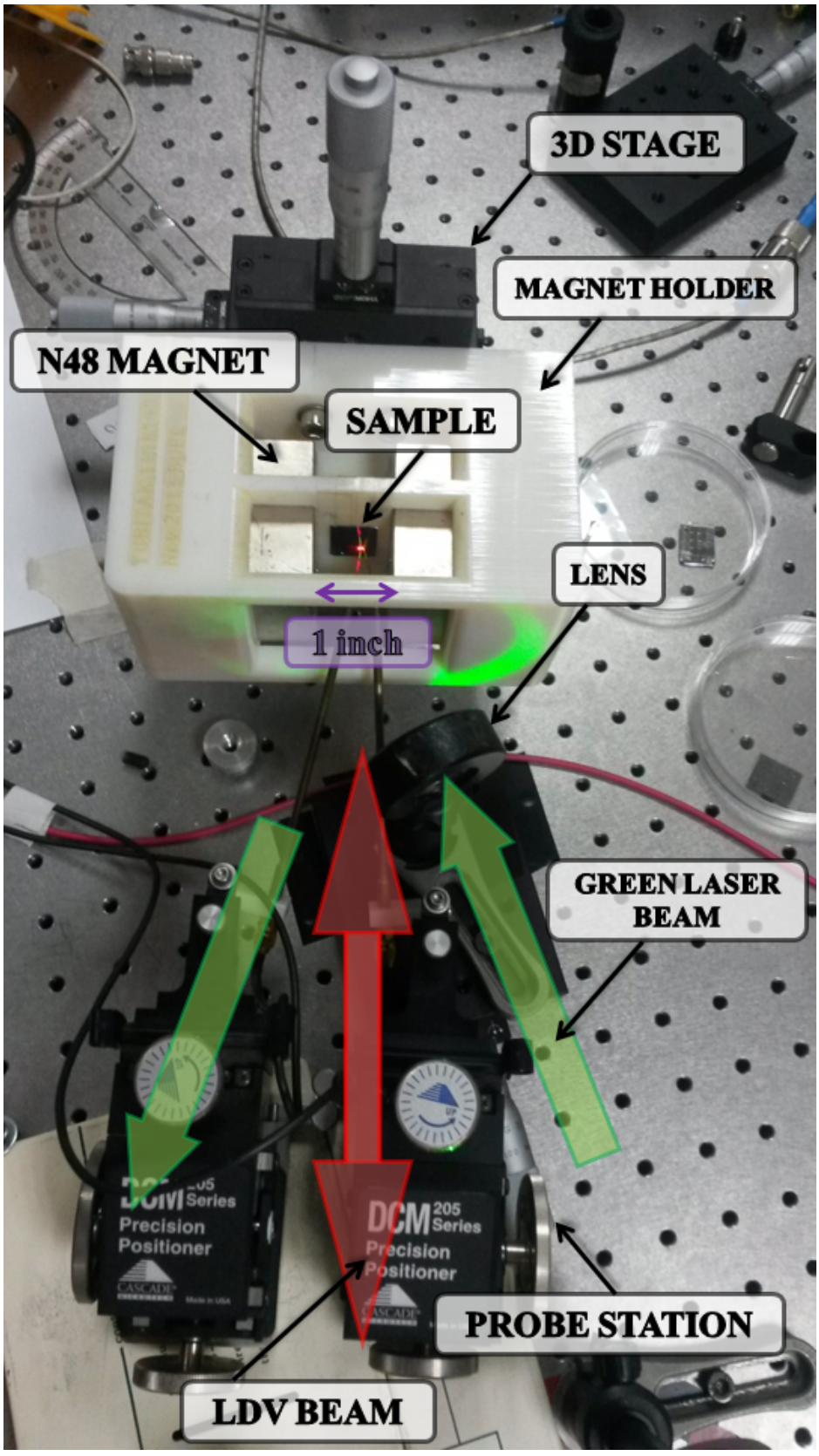

Figure 4.3. Top view from the characterization setup.

The LDV laser is emitted perpendicular to the mirror of the resonator from a laser gun placed on a 3D stage. The tip of the LDV laser gun should be placed 30 cm away from the sample and fine tuned on the vibrating resonator. It detects the velocity with a resolution of 100 $mm/s/V$ and its output is directed to the spectrum analyzer. Once the magnetic field is provided and the probes are down, having a resistance of 50 ohms for the resonator, it is time to pass the electrical current through the resonator and detect the induced mechanical vibration. The resonators are characterized having their electrical current either driven by an external function generator or driven by the CMOS IC. In the first phase of the characterization, devices are characterized by generating the electrical current passing through the resonators using an external function generator. Figure 4.4 shows the resonance frequency response of a number of resonators with different dimensions. Table 4.1 demonstrates the resonance frequencies from FEM simulations and characterization, SNR values, quality factor, and the RMS value of the electrical currents.

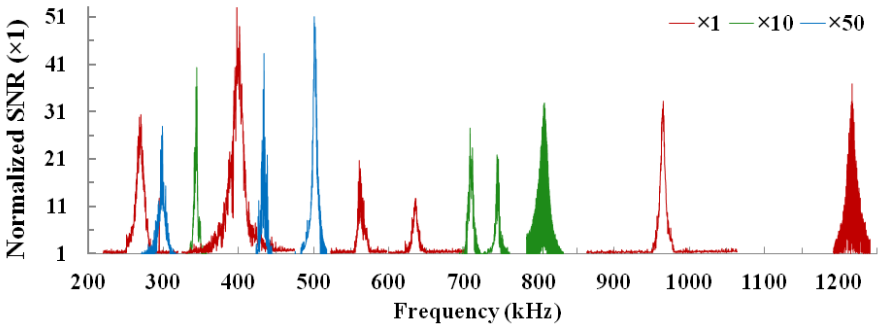

Figure 4.4. The resonance frequency response of a number of resonators characterized by the electrical current driven by an external function generator.

In the second phase of the characterization, devices are characterized by generating the resonator current by the CMOS IC. Figure 1.10 shows how the resonator is been driven by the CMOS IC. The frequency response of a number of devices driven by the CMOS IC is shown in Figure 4.5. The detailed characteristics of the charac-

terization results are demonstrated in Table 4.2. In the first resonator, the current is directly driven by the CMOS IC having the RMS value of 25 μA. But, in the rest of the resonators the current is amplified by a transimpedance amplifier. The values of amplified current is shown in the last column of Table 4.2.

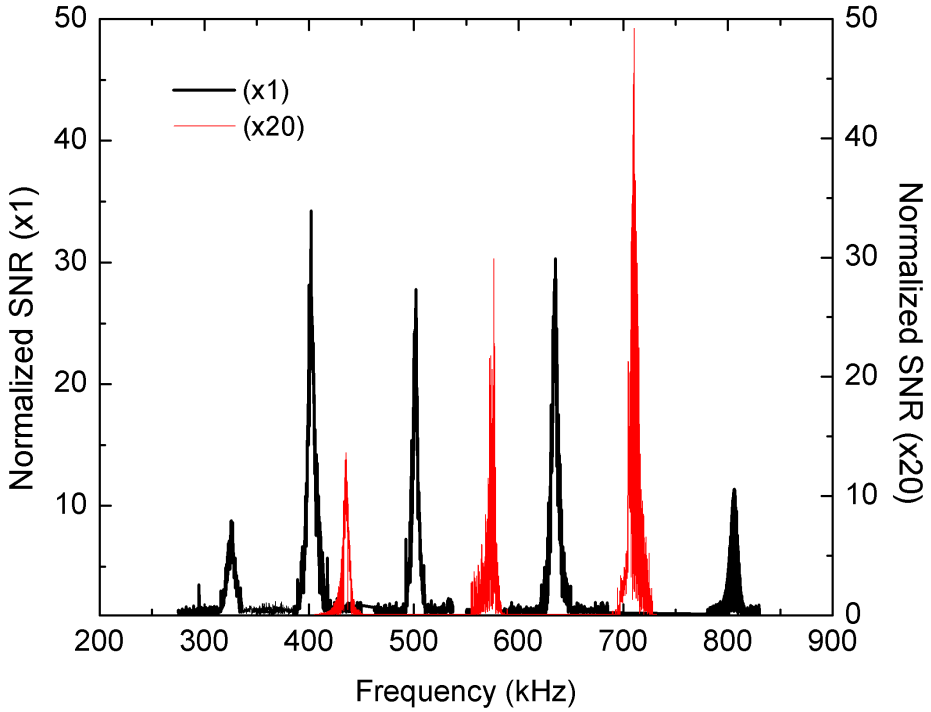

Figure 4.5. The resonance frequency response of a number of resonators characterized by the electrical current driven by the CMOS IC.

Figure 4.4 and 4.5 show the normalized SNR of the frequency responses that are characterized with different electrical currents. They are helpful in depicting the whole range of the frequency and the contribution of each device in covering certain range of frequency. However, since the electrical currents are different, it is not possible to sum up all the frequency responses in one diagram and show the absolute value of the maximum displacement and indicate the minimum detection level. However, Figure 4.6 shows the absolute values of the received power from LDV, maximum velocity, and the maximum displacement of a single device (number 8 from Table 2.2). It presents a resonance frequency at 325 kHz with the electrical current driven by the CMOS IC (nominal current value of 25 μA- RMS). More characterization details can be found

in Table 4.2 regarding the above mentioned device (see resonator number 1).

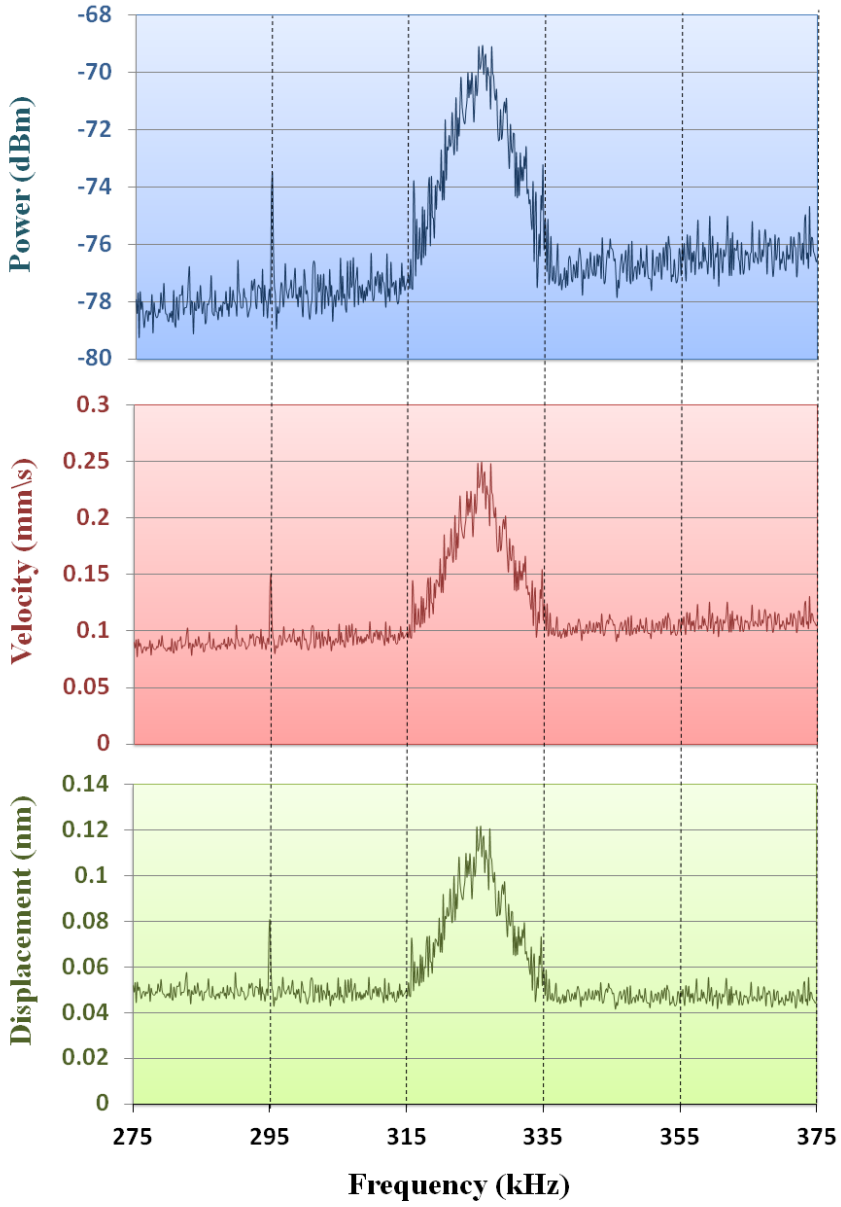

Figure 4.6. The absolute values of the received power from LDV (top), maximum velocity (middle), and the maximum displacement (down) of a single device (number 8 from Table 2.2 and number 1 from Table 4.2).

Table 4.1. The detailed characterization results for the devices driven by the external function generator.

Resonator number	Resonance frequency from simulation (kHz)	Resonance frequency from characterization (kHz)	Relative error (%)	Quality factor	Driving current (mA- RMS)
1	247	270	9.3	24.5	3.2
2	294	296	0.7	37.5	2
3	280	340	21.4	113.3	2
4	325	398	22.4	28.5	1.4
5	417	433	3.8	86.6	2
6	432	502	16.2	71.7	2
7	535	560	4.7	56	4
8	624	635	1.8	105.8	2.6
9	645	707	9.6	101	2
10	691	740	7	123.3	2
11	751	807	7.5	67.25	2
12	997	965	3.2	120.6	2
13	1480	1210	18.2	86.4	2

Table 4.2. The detailed characterization results for the devices driven by the CMOS IC.

Resonator number	Resonance frequency from simulation (kHz)	Resonance frequency from characterization (kHz)	Relative error (%)	Quality factor	Driving current (μA- RMS)
1	268	325	21.3	35	25
2	325	402	23.7	77.3	3800
3	417	435	4.3	87.1	360
4	431	502	16.5	143.4	250
5	535	575	7.5	192	4500
6	624	635	1.8	127	3800
7	645	710	10	88.7	4500
8	751	805	7.2	115	4500

5. CONCLUSION AND FUTURE WORK

In this thesis, RF MEMS resonators are fabricated by electroplating nickel as the structural layer. A number of substrates and seed layers are tested and eventually copper is chosen. A thin layer of titanium is used for adhesion promoter between the copper and the substrate. Glass substrates are tested initially and are shown to be functioning. However, the eventual devices are fabricated on silicon wafer as substrate.

The resonators are characterized and shown to be functioning over the entire range that are designed for (150 kHz to 1.5 MHz) with relative errors lower than 25 percent comparing with FEM simulation results. Also, they are partly characterized having their electrical current being driven from the CMOS IC which is powered optically. It is shown that resonators can indeed function with the small current of 25 muA- RMS driven by the CMOS IC and respond with an SNR of 10 dB. The minimum detectable level for displacement is measured to be 50 pm. The power of the resonance frequency response would extensively increase under MRI environment; because, there will be a five times stronger DC magnetic field than the magnetic field present in our characterization setup. To show this extensive increase, the devices are characterized by a range of higher current values whether by an external function generator or a transimpedance amplifier amplifying the current driven by CMOS IC.

For future work, first of all, the present fabricated devices need be characterized by DGI. Second,, the six resonators which can be characterized by DGI are all similar in dimensions having resonance frequencies close to 300 kHz. If the the final system is going to employ DGI as the the optical readout method all the devices with different dimensions and resonance frequencies should be redesigned with diffraction grated mirrors to cover the entire necessary range of resonance frequecnies. Otherwise, relying on LDV for the optical readout let us stay with the present design.

Also, the configuration of the resonators are to be redesigned to make bigger families to cover the entire range of resonance frequencies all integrated into one family

and coupled to the fiber optic cable. It is beneficial to mention that to be able to electroplate thicker structural layers more than 1.5 μm the positive PR can be changed with a negative PR and/or the mask can be modified to a dark field mask.

Once the design configuration is fabricated and characterized, the CMOS IC and the MEMS sensor array should have to get integrated and both have to become packaged and coupled to fiber optic cables for optical power input and optical readout. Finally, the whole catheter tracking system has to be tested under MRI environment.

REFERENCES

1. Reaungamornrat, S., Y. Otake, A. Uneri, S. Schafer, J. Stayman, W. Zbijewski, D. Mirota, J. Yoo, S. Nithiananthan and A. Khanna, "Tracker-On-C: A Novel Tracker Configuration for Image-Guided Therapy using a Mobile C-Arm", *Computer Assisted Radiology and Surgery, Berlin, Germany*, pp. 22–25, 2011.

2. Glossop, N. D., "Advantages of Optical Compared with Electromagnetic Tracking", *The Journal of Bone & Joint Surgery*, Vol. 91, No. Supplement_1, pp. 23–28, 2009.

3. Paquit, V., J. R. Price, R. Seulin, F. Mériaudeau, R. H. Farahi, K. W. Tobin Jr and T. L. Ferrell, "Near-Infrared Imaging and Structured Light Ranging for Automatic Catheter Insertion", *Medical Imaging*, pp. 61411T–61411T, International Society for Optics and Photonics, 2006.

4. Slabaugh, G., K. Kong, G. Unal and T. Fang, "Variational Guidewire Tracking using Phase Congruency", *Medical Image Computing and Computer-Assisted Intervention–MICCAI 2007*, pp. 612–619, Springer, 2007.

5. Rex, J. A., *Catheter Tracking System*, US Patent 6,298,261, 2001.

6. Gubbels, A. W., W. L. Smith and I. Vesely, *Three-Dimensional Digital Ultrasound Tracking System*, US Patent 5,515,853, 1996.

7. Seiler, P., H. Blattmann, S. Kirsch, R. Muench and C. Schilling, "A Novel Tracking Technique for the Continuous Precise Measurement of Tumour Positions in Conformal Radiotherapy", *Physics in medicine and biology*, Vol. 45, No. 9, p. N103, 2000.

8. Wacker, F. K., D. Elgort, C. M. Hillenbrand, J. L. Duerk and J. S. Lewin, "The Catheter-Driven MRI Scanner: a New Approach to Intravascular Catheter Track-

ing and Imaging-Parameter Adjustment for Interventional MRI", *American Journal of Roentgenology*, Vol. 183, No. 2, pp. 391–395, 2004.

9. Cakaci, A. U., *An Electromagnetic MEMS-Based Resonator Design for Catheter Tracking in MRI*, M.S. Thesis, Bogazici University, 2013.

10. Pai, R. S., "Nickel Electroplating using Shipley Megaposit SPR 220 Positive Resist as a Mold", `http://www.tex.stackexchange.com` , 2001, [Accessed August 2014].

11. Luo, J., A. Flewitt, S. Spearing, N. Fleck and W. Milne, "Youngs Modulus of Electroplated Ni Thin Film for MEMS Applications", *Materials Letters*, Vol. 58, No. 17, pp. 2306–2309, 2004.

12. Birkfellner, W., J. Hummel, E. Wilson and K. Cleary, "Tracking Devices", *Image-Guided Interventions*, pp. 23–44, Springer, 2008.

13. "Reduction Potentials", `http://www.chem.wisc.edu` , 2014, [Accessed August 2014].

14. Yalcinkaya, A. D., *Development of an Electromagnetic MEMS Based, Interventional MRI Compatible Real-Time Localization Microsystem with All-Optical Communication*, Project Proposal for TUBITAK, 2011.

15. Colchester, A. C., J. Zhao, K. S. Holton-Tainter, C. J. Henri, N. Maitland, P. T. Roberts, C. G. Harris and R. J. Evans, "Development and Preliminary Evaluation of VISLAN, a Surgical Planning and Guidance System using Intra-Operative Video Imaging", *Medical Image Analysis*, Vol. 1, No. 1, pp. 73–90, 1996.

16. Kato, H. and M. Billinghurst, "Marker Tracking and HMD Calibration for a Video-Based Augmented Reality Conferencing System", *Augmented Reality, 1999.(IWAR'99) Proceedings. 2nd IEEE and ACM International Workshop on*, pp. 85–94, IEEE, 1999.

17. Ross, A. J., *Retro-Reflective Particles and Reflective Markers and Compositions Containing Such Particles*, US Patent 3,254,563, 1966.

18. De Buck, S., J. Ector, A. La Gerche, F. Maes, H. Heidbuchel *et al.*, "Toward Image-Based Catheter Tip Tracking for Treatment of Atrial Fibrillation", *CI2BM09-MICCAI Workshop on Cardiovascular Interventional Imaging and Biophysical Modelling*, 2009.

19. Honnorat, N., R. Vaillant and N. Paragios, "Guide-Wire Extraction Through Perceptual Organization of Local Segments in Fluoroscopic Images", *Medical Image Computing and Computer-Assisted Intervention–MICCAI 2010*, pp. 440–448, Springer, 2010.

20. Ma, Y., N. Gogin, P. Cathier, R. J. Housden, G. Gijsbers, M. Cooklin, M. O'Neill, J. Gill, C. A. Rinaldi, R. Razavi *et al.*, "Real-Time X-Ray Fluoroscopy-Based Catheter Detection and Tracking for Cardiac Electrophysiology Interventions", *Medical physics*, Vol. 40, No. 7, p. 071902, 2013.

21. Schenderlein, M., V. Rasche and K. Dietmayer, "Three-Dimensional Catheter Tip Tracking From Asynchronous Biplane X-Ray Image Sequences using Non-Linear State Filtering", *Bildverarbeitung für die Medizin 2011*, pp. 234–238, Springer, 2011.

22. Aubin, S., L. Beaulieu, S. Pouliot, J. Pouliot, R. Roy, L.-M. Girouard, N. Martel-Brisson, E. Vigneault and J. Laverdiere, "Robustness and Precision of an Automatic Marker Detection Algorithm for Online Prostate Daily Targeting using a Standard V-EPID", *Medical physics*, Vol. 30, No. 7, pp. 1825–1832, 2003.

23. Pouliot, J., M. Aubin, K. M. Langen, Y.-M. Liu, B. Pickett, K. Shinohara and M. Roach III, "(Non)-Migration of Radiopaque Markers used for On-Line Localization of the Prostate with an Electronic Portal Imaging Device", *International Journal of Radiation Oncology* Biology* Physics*, Vol. 56, No. 3, pp. 862–866, 2003.

24. Harada, T., H. Shirato, S. Ogura, S. Oizumi, K. Yamazaki, S. Shimizu, R. Onimaru, K. Miyasaka, M. Nishimura and H. Dosaka-Akita, "Real-Time Tumor-Tracking Radiation Therapy for Lung Carcinoma by the Aid of Insertion of a Gold Marker using Bronchofiberscopy", *Cancer*, Vol. 95, No. 8, pp. 1720–1727, 2002.

25. Nederveen, A., J. Lagendijk and P. Hofman, "Feasibility of Automatic Marker Detection with an A-Si Flat-Panel Imager", *Physics in medicine and biology*, Vol. 46, No. 4, p. 1219, 2001.

26. Pang, G., D. Beachey, P. O'Brien and J. Rowlands, "Imaging of 1.0-mm-Diameter Radiopaque Markers with Megavoltage X-Rays: an Improved Online Imaging System", *International Journal of Radiation Oncology* Biology* Physics*, Vol. 52, No. 2, pp. 532–537, 2002.

27. Shimizu, S., H. Shirato, K. Kitamura, N. Shinohara, T. Harabayashi, T. Tsukamoto, T. Koyanagi and K. Miyasaka, "Use of an Implanted Marker and Real-Time Tracking of the Marker for the Positioning of Prostate and Bladder Cancers", *International Journal of Radiation Oncology* Biology* Physics*, Vol. 48, No. 5, pp. 1591–1597, 2000.

28. Vetterli, D., S. Thalmann, F. Behrensmeier, L. Kemmerling, E. J. Born, R. Mini, R. H. Greiner and D. M. Aebersold, "Daily Organ Tracking in Intensity-Modulated Radiotherapy of Prostate Cancer using an Electronic Portal Imaging Device with a Dose Saving Acquisition Mode", *Radiotherapy and oncology*, Vol. 79, No. 1, pp. 101–108, 2006.

29. Baert, S. A., M. A. Viergever and W. J. Niessen, "Guide-Wire Tracking During Endovascular Interventions", *Medical Imaging, IEEE Transactions on*, Vol. 22, No. 8, pp. 965–972, 2003.

30. Van Walsum, T., S. A. Baert and W. J. Niessen, "Guide Wire Reconstruction and Visualization in 3DRA using Monoplane Fluoroscopic Imaging", *Medical Imaging,*

IEEE Transactions on, Vol. 24, No. 5, pp. 612–623, 2005.

31. Mori, K., D. Deguchi, J. Sugiyama, Y. Suenaga, J.-i. Toriwaki, C. R. Maurer Jr, H. Takabatake and H. Natori, "Tracking of a Bronchoscope using Epipolar Geometry Analysis and Intensity-Based Image Registration of Real and Virtual Endoscopic Images", *Medical Image Analysis*, Vol. 6, No. 3, pp. 321–336, 2002.

32. van de Kraats, E. B., T. v. Walsum, L. Kendrick, N. J. Noordhoek and W. J. Niessen, "Accuracy Evaluation of Direct Navigation with an Isocentric 3D Rotational X-Ray System", *Medical image analysis*, Vol. 10, No. 2, pp. 113–124, 2006.

33. Russakoff, D. B., T. Rohlfing, K. Mori, D. Rueckert, A. Ho, J. R. Adler Jr and C. R. Maurer Jr, "Fast Generation of Digitally Reconstructed Radiographs using Attenuation Fields with Application to 2D-3D Image Registration", *Medical Imaging, IEEE Transactions on*, Vol. 24, No. 11, pp. 1441–1454, 2005.

34. Russakoff, D. B., T. Rohlfing, D. Rueckert, R. Shahidi, D. Kim and C. R. Maurer Jr, "Fast Calculation of Digitally Reconstructed Radiographs using Light Fields", *Medical Imaging 2003*, pp. 684–695, International Society for Optics and Photonics, 2003.

35. Russakoff, D. B., T. Rohlfing and C. R. Maurer Jr, "Fast Intensity-Based 2D-3D Image Registration of Clinical Data using Light", *Computer Vision, 2003. Proceedings. Ninth IEEE International Conference on*, pp. 416–422, IEEE, 2003.

36. Kleinerman, R. A., "Cancer Risks Following Diagnostic and Therapeutic Radiation Exposure in Children", *Pediatric radiology*, Vol. 36, No. 2, pp. 121–125, 2006.

37. Yu, S.-B. and A. D. Watson, "Metal-Based X-Ray Contrast Media", *Chemical reviews*, Vol. 99, No. 9, pp. 2353–2378, 1999.

38. Rabin, O., J. M. Perez, J. Grimm, G. Wojtkiewicz and R. Weissleder, "An X-Ray Computed Tomography Imaging Agent Based on Long-Circulating Bismuth Sulphide Nanoparticles", *Nature materials*, Vol. 5, No. 2, pp. 118–122, 2006.

39. Tweedle, M. F. and K. Kumar, "Magnetic Resonance Imaging (MRI) Contrast Agents", *Metallopharmaceuticals II*, pp. 1–43, Springer, 1999.

40. Cooperberg, P. L., J. J. Barberie, T. Wong and C. Fix, "Extended Field-of-View Ultrasound", *Seminars in Ultrasound, CT and MRI*, Vol. 22, pp. 65–77, Elsevier, 2001.

41. Weng, L., A. P. Tirumalai, C. M. Lowery, L. F. Nock, D. E. Gustafson, P. Von Behren and J. H. Kim, "US Extended-Field-of-View Imaging Technology.", *Radiology*, Vol. 203, No. 3, pp. 877–880, 1997.

42. Smith, W. and I. Vesely, *Method for Carrying out a Medical Procedure using a Three-Dimensional Tracking and Imaging System*, US Patent 5,797,849, 1998.

43. LaScalza, S., J. Arico and R. Hughes, "Effect of Metal and Sampling Rate on Accuracy of Flock of Birds Electromagnetic Tracking System", *Journal of biomechanics*, Vol. 36, No. 1, pp. 141–144, 2003.

44. Stevens, F., M. A. Conditt, N. Kulkarni, S. K. Ismaily, P. C. Noble and D. R. Lionberger, "Minimizing Electromagnetic Interference from Surgical Instruments on Electromagnetic Surgical Navigation", *Clinical Orthopaedics and Related Research®*, Vol. 468, No. 8, pp. 2244–2250, 2010.

45. Wood, B. J., H. Zhang, A. Durrani, N. Glossop, S. Ranjan, D. Lindisch, E. Levy, F. Banovac, J. Borgert, S. Krueger *et al.*, "Navigation with Electromagnetic Tracking for Interventional Radiology Procedures: a Feasibility Study", *Journal of vascular and interventional radiology*, Vol. 16, No. 4, pp. 493–505, 2005.

46. Pan, L., J. Barbot, S. Shea, S. Patil, K. Kirchberg, G. Meredith, T. Meng, E. Khol-

movski, S. Vijayakumar and K. Vij, "An Integrated System for Catheter Tracking and Visualization in MR-Guided Cardiovascular Interventions", *Proc. Intl. Soc. Mag. Reson. Med*, Vol. 19, p. 195, 2011.

47. Darrow, R. D., C. L. Dumoulin, J. F. Schenck and S. P. Souza, *Tracking System to Follow the Position and Orientation of a Device with Radiofrequency Field Gradients*, US Patent 5,211,165, 1993.

48. Shellock, F. G., "Radiofrequency Energy-Induced Heating During MR Procedures: A Review", *Journal of Magnetic Resonance Imaging*, Vol. 12, No. 1, pp. 30–36, 2000.

49. Yeung, C. J., R. C. Susil and E. Atalar, "RF Safety of Wires in Interventional MRI: Using a Safety Index", *Magnetic Resonance in Medicine*, Vol. 47, No. 1, pp. 187–193, 2002.

50. Konings, M. K., L. W. Bartels, H. F. M. Smits and C. J. G. Bakker, "Heating Around Intravascular Guidewires by Resonating RF Waves", *Journal of Magnetic Resonance Imaging*, Vol. 12, No. 1, pp. 79–85, 2000.

51. Nyenhuis, J. A., S. M. Park and R. Kamondetdacha, "MRI and Implanted Medical Devices: Basic Interactions with an Emphasis on Heating", *IEEE Transactions on Device and Materials Reliability*, Vol. 5, No. 3, pp. 467–480, 2005.

52. Shellock, F. G., *Magnetic Resonance Procedures: Health Effects and Safety*, CRC Press, Boca Raton, 2001.

53. Ladd, M. E. and H. H. Quick, "Reduction of Resonant RF Heating in Intravascular Catheters using Coaxial Chokes", *Magnetic resonance in medicine*, Vol. 43, No. 4, pp. 615–619, 2000.

54. Weiss, S., P. Vernickel, T. Schaeffter, B. Gleich and V. Schulz, "Towards an RF-Safe Active Catheter for MR-Guided Interventions", *Kontraste (Hamburg)*,

Vol. 49, No. 3, pp. 48–53, 2005.

55. Konings, M., S. Weiss, C. Bakker, L. Bartels and W. Mali, "Catheters and Guidewires in Interventional MRI: Problems and Solutions", *Medicamundi*, Vol. 45, No. 1, pp. 31–39, 2001.

56. Muller, L., M. Saeed, M. W. Wilson and S. W. Hetts, "Remote Control Catheter Navigation: Options for Guidance under MRI", *Journal of Cardiovascular Magnetic Resonance*, Vol. 14, No. 1, p. 33, 2012.

57. Bushong, S. C., *Magnetic Resonance Imaging: Physical and Biological Principles*, Mosby, St. Louis, 2003.

58. Wu, M. C., O. Solgaard and J. E. Ford, "Optical MEMS for lightwave communication", *Lightwave Technology, Journal of*, Vol. 24, No. 12, pp. 4433–4454, 2006.

59. Nallani, A. K., T. Chen, D. J. Hayes, W.-S. Che and J.-B. Lee, "A Method for Improved VCSEL Packaging using MEMS and Ink-Jet Technologies", *Lightwave Technology, Journal of*, Vol. 24, No. 3, pp. 1504–1512, 2006.

60. Savastano, L., G. Maier, A. Pattavina and M. Martinelli, "Physical-Parameter Design in 2-D MEMS Optical Switches", *Lightwave Technology, Journal of*, Vol. 23, No. 10, pp. 3147–3155, 2005.

61. Lee, S.-S., L.-S. Huang, C.-J. Kim and M. C. Wu, "Free Space Fiber Optic Switches Based on MEMS Vertical Torsion Mirrors", *Journal of lightwave technology*, Vol. 17, No. 1, p. 7, 1999.

62. Veladi, H., R. R. Syms and H. Zou, "Fiber-Pigtailed Electrothermal MEMS Iris VOA", *Journal of lightwave technology*, Vol. 25, No. 8, pp. 2159–2167, 2007.

63. Lee, C., "A MEMS VOA using Electrothermal Actuators", *Journal of lightwave technology*, Vol. 25, No. 2, pp. 490–498, 2007.

64. Yu, K., D. Lee, N. Park and O. Solgaard, "Tunable Optical Bandpass Filter with Variable-Aperture MEMS Reflector", *Journal of lightwave technology*, Vol. 24, No. 12, pp. 5095–5102, 2006.

65. Tsai, C.-W., H.-T. Chang, S.-H. Liu and J.-c. Tsai, "Magnetically-Actuated Swing-Type MEMS Mirror Pair for a Reconfigurable Optical Interconnect", *Journal of Lightwave Technology*, Vol. 31, No. 24, pp. 4126–4134, 2013.

66. Putrino, G., A. Keating, M. Martyniuk, L. Faraone and J. Dell, "Model and Analysis of a High Sensitivity Resonant Optical Read-Out Approach Suitable for Cantilever Sensor Arrays", *Journal of Lightwave Technology*, Vol. 30, No. 12, pp. 1863–1868, 2012.

67. Sarioglu, B., M. Tumer, U. Cindemir, B. Camli, G. Dundar, C. Ozturk and A. D. Yalcinkaya, "An Optically Powered CMOS Tracking System for 3 T Magnetic Resonance Environment", *Biomedical Circuits and Systems, IEEE Transactions on*, Vol. PP, No. 99, pp. 1–1, 2014.

68. Bao, M.-H., *Analysis and Design Principles of MEMS Devices*, Elsevier, London, 2005.

69. Urey, H., C. Kan and W. O. Davis, "Vibration Mode Frequency Formulae for Micromechanical Scanners", *Journal of Micromechanics and Microengineering*, Vol. 15, No. 9, p. 1713, 2005.

70. Di Bari, J., "Electrodeposition of Nickel", *Modern Electroplating*, pp. 79–114, 2000.

71. "Kinds of Chemical Changes", `http://www.chem.wisc.edu` , 2014, [Accessed August 2014].